

Industrial-era decline in subarctic Atlantic productivity

Matthew B. Osman^{1*}, Sarah B. Das², Luke D. Trusel³, Matthew J. Evans⁴, Hubertus Fischer⁵, Mackenzie M. Grieman⁶, Sepp Kipfstuhl⁷, Joseph R. McConnell⁸ & Eric S. Saltzman⁶

Marine phytoplankton have a crucial role in the modulation of marine-based food webs¹, fishery yields² and the global drawdown of atmospheric carbon dioxide³. However, owing to sparse measurements before satellite monitoring in the twenty-first century, the long-term response of planktonic stocks to climate forcing is unknown. Here, using a continuous, multi-century record of subarctic Atlantic marine productivity, we show that a marked $10 \pm 7\%$ decline in net primary productivity has occurred across this highly productive ocean basin over the past two centuries. We support this conclusion by the application of a marine-productivity proxy, established using the signal of the planktonic-derived aerosol methanesulfonic acid, which is commonly identified across an array of Greenlandic ice cores. Using contemporaneous satellite-era observations, we demonstrate the use of this signal as a robust and high-resolution proxy for past variations in spatially integrated marine productivity. We show that the initiation of declining subarctic Atlantic productivity broadly coincides with the onset of Arctic surface warming⁴, and that productivity strongly covaries with regional sea-surface temperatures and basin-wide gyre circulation strength over recent decades. Taken together, our results suggest that the decline in industrial-era productivity may be evidence of the predicted⁵ collapse of northern Atlantic planktonic stocks in response to a weakened Atlantic Meridional Overturning Circulation^{6–8}. Continued weakening of this Atlantic Meridional Overturning Circulation, as projected for the twenty-first century^{9,10}, may therefore result in further productivity declines across this globally relevant region.

The subarctic Atlantic (50–65° N, 60–10° W) comprises one of the world's most biologically productive seasonal phytoplankton blooms^{11–14}. Bloom magnitude varies annually, in response to controls such as the timing and abundance of light and nutrients in the upper ocean^{12,13}, and predator–prey coupling dynamics¹⁴. These biophysical controls, in turn, vary in response to underlying physical drivers that are sensitive to long-term changes in upper-ocean climatic forcing, such as the depth of the mixed layer, sea-surface temperature (SST), baroclinicity and wind.

Over the preceding 200 years (that is, the industrial era), the northern Atlantic has undergone numerous climatic perturbations outside the range of naturally forced variability, resulting in widespread surface warming⁴, slowdown of the Atlantic Meridional Overturning Circulation (AMOC)^{6–8}, declines in sea ice¹⁵ and accelerating Greenland Ice Sheet (GrIS) runoff¹⁶. Contemporaneous estimates of primary productivity are less well resolved. Satellite-derived concentrations of planktonic biomass, extending back only to late 1997 (and intermittently to 1979)^{11,12}, do not reveal significant decadal-scale trends, but rather, modest productivity variability over the first two decades of monitoring during the twenty-first century (Extended Data Figs. 1, 2 and Supplementary Information). Previous spatiotemporally

sparse sources, including ship-based ocean colour¹¹ and planktonic abundance observations¹⁷ (Extended Data Fig. 3 and Supplementary Information), however, hint at a longer-term decline during the twentieth century. To our knowledge, no spatially reconciled, temporally resolved reconstruction of basin-scale primary productivity currently exists that includes the pre- to post-industrial transition. This limits our ability to quantify climatic impacts on subarctic Atlantic ecosystems and contextualize model-based predictions of future ecologic responses to anthropogenic forcing⁹.

Here we use records of a marine-derived biogenic aerosol (the concentration of methanesulfonic acid ([MSA])) from GrIS ice cores to reconstruct annual variability in productivity across the subarctic Atlantic over the preceding two and a half centuries. At high latitudes, MSA is solely produced as an oxidative byproduct from oceanic dimethylsulfide (DMS) emissions¹⁸. DMS, in turn, is linked to several planktonic life-cycle processes that involve assemblages of dinoflagellates, haptophytes (including coccolithophores) and, to a lesser extent, diatoms, chrysophytes and prasinophytes¹⁹. Notwithstanding uncertainties in the long-term feedback effects between DMS emissions and climate²⁰, we demonstrate that GrIS [MSA] records provide a first-order proxy for regional ocean–atmosphere fluxes of DMS¹⁸ (Methods), which are tightly coupled to changes in nearby marine productivity²¹.

We combine 12 high-resolution [MSA] records (Methods) to examine the covariation of [MSA] across the GrIS (Extended Data Table 1). To physically constrain potential source regions of DMS emissions across the 12 ice core sites, we conduct daily atmospheric back-trajectory analyses during the time of the MSA summertime maximum, June–July–August (JJA; Extended Data Table 1), over a multidecadal time-frame (AD 1948–2013; Methods). A conspicuous multi-century decline in [MSA] is evident in nearly all records (Fig. 1a), irrespective of their GrIS locations and primary summertime airmass-trajectory pathways—trending from a predominantly southeasterly dominated atmospheric influence (originating in the Irminger Sea) at southern GrIS sites to a southwesterly dominated influence (originating in the Labrador Sea) at northern sites (Fig. 1b and Extended Data Figs. 4, 5). Moreover, when averaging the 12 records into either Irminger Sea-dominated constituents ($n = 7$ sites; Fig. 1b) or Labrador Sea-dominated constituents ($n = 5$ sites), we find significant GrIS [MSA] covariation down to annual timescales ($P < 0.0001$; Extended Data Fig. 6 and Supplementary Information).

This strong coherence suggests that time variability of MSA deposition across the GrIS is dominated by a common, large-scale mode of DMS production and emissions across the North Atlantic. Using a probabilistic principal component analysis, we extract this common signal of GrIS [MSA] variability over the period AD 1767–2013 (Methods). The leading principal component ([MSA] PC1) robustly captures the multi-century decline in the industrial-era [MSA] that is observed across the individual records, while significantly ($P = 0.002$)

¹Massachusetts Institute of Technology and Woods Hole Oceanographic Institution Joint Program in Oceanography and Applied Ocean Sciences and Engineering, Woods Hole, MA, USA.

²Department of Geology and Geophysics, Woods Hole Oceanographic Institution, Woods Hole, MA, USA. ³Department of Geology, Rowan University, Glassboro, NJ, USA. ⁴Department of Chemistry, Wheaton College, Norton, MA, USA. ⁵Climate and Environmental Physics, Physics Institute and Oeschger Centre for Climate Change Research, University of Bern, Bern, Switzerland. ⁶Department of Earth System Science, University of California, Irvine, Irvine, CA, USA. ⁷Alfred-Wegener-Institute, Bremerhaven, Germany. ⁸Division of Hydrologic Sciences, Desert Research Institute, Reno, NV, USA.

*e-mail: osmanm@mit.edu

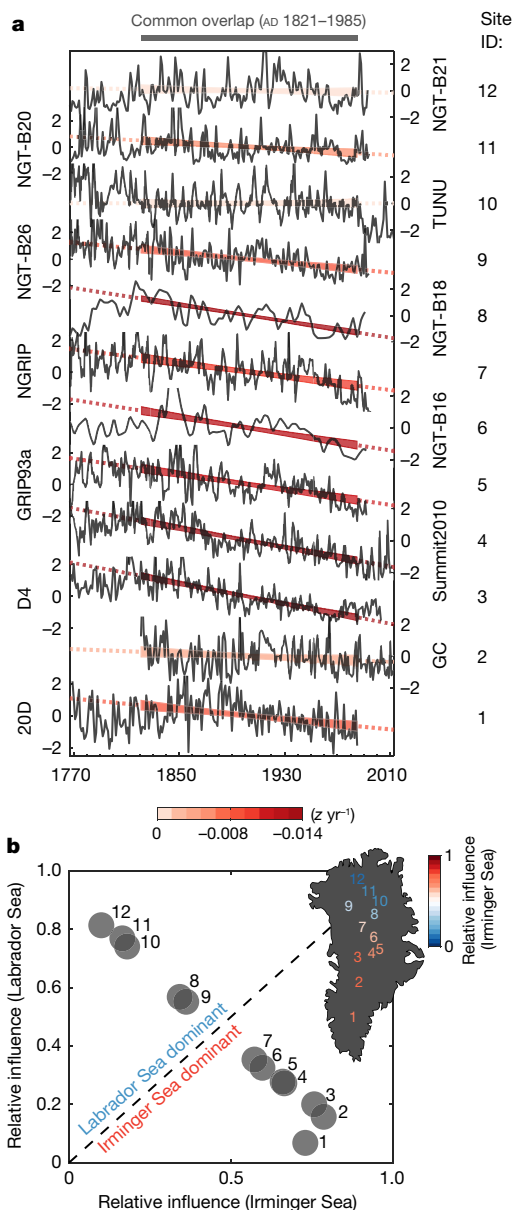


Fig. 1 | Strong covariability between Greenlandic [MSA] records.

a, The 12 individual [MSA] time series, plotted from most southerly situated (bottom; 20D) to most northerly situated (top; NGT-B21). All series are standardized relative to AD 1821–1885 (the period of common overlap; in z -units) with linear [MSA] trends computed for the overlapping AD 1821–1885 period. Shaded red envelopes denote the 90% confidence intervals of the regressions during the period of common overlap and the dotted lines show extension of the regressions beyond this period. Note the site identification numbers to the right of the time series. **b**, Communality scores for the hybrid single-particle Lagrangian integrated trajectory (HYSPLIT)-derived air mass transport density maps of the 12 sites (see Methods; Fig. 2 and Extended Data Fig. 4) following factor analysis with varimax rotation (Supplementary Information). Sites are grouped by whether their incoming marine air masses are derived predominantly from the Irminger Sea (factor 1; x axis) or Labrador Sea (factor 2; y axis). Locations of the 12 sites on the GrIS are provided in the inset, with each site identifier colour-coded with respect to its factor 1 communality score (that is, relative influence of the Irminger Sea). Ice core sites influenced predominantly by air masses originating from the Irminger Sea are denoted using red hues ($n = 7$) and sites that are predominantly influenced by the Labrador Sea are denoted using blue hues ($n = 5$; Extended Data Fig. 6).

explaining nearly half of the GrIS [MSA] variability (median or mode at around 44%; Fig. 2a). Correlation of the [MSA] records to the resultant [MSA] PC1 signal furthermore reveals each record to be significantly

and positively related ($P < 0.1$; Methods and Extended Data Table 1), with centrally situated GrIS sites exhibiting the strongest covariation with [MSA] PC1 (Fig. 2a). Exploiting this spatial-loading pattern, we statistically combine the back-trajectory results for the 12 sites (Methods; Extended Data Figs. 4, 5) and find that the west-central to northeastern subarctic Atlantic basin is the most probable source of GrIS-deposited MSA (Fig. 2b, c). Notably, this MSA source region, centred over the highly productive^{1,12,17} and climatically sensitive^{1,6–8,22} Irminger and Labrador Seas proximal to the upwind Greenland coast, overlaps with the greatest Atlantic-sector surface JJA DMS seawater concentrations²³ ([DMS_{SW}]) and, relatedly, DMS emissions (Fig. 3a).

Furthermore, strong spatial coherence exists between summertime [DMS_{SW}] and satellite-derived estimates of net primary productivity (NPP) from the chlorophyll- α -dependent Vertically Generalized Production Model¹² (VGPM; Supplementary Information) across the northern Atlantic sector, despite differences in the collection and spatial scalability of these two data sources (Fig. 3a and Methods). The observed similarity suggests that past variations in northern Atlantic DMS production, as inferred from [MSA] PC1, also provide a signal of past productivity variations across this sector, given time-averaged scalability in the ocean–atmosphere emission rate of DMS to DMS_{SW} production²³. Indeed, correlations between VGPM-derived NPP and [DMS_{SW}] measurements from the NOAA Global Surface Seawater DMS database²³ (Methods) support a strong spatiotemporal association ($r = 0.75$) between subarctic Atlantic productivity and the magnitude of DMS production (Fig. 3b), a relationship well above globally integrated values (Extended Data Fig. 7c and Supplementary Information). A similar regression analysis against independently derived counts of DMS-producing diatom, dinoflagellate and coccolithophore abundance from the Continuous Plankton Recorder (CPR) ship survey (Methods) also yields significant relationships with [DMS_{SW}] in all three functional groups ($P < 0.005$; Extended Data Fig. 7d–f), indicating that variations in DMS production and emissions across the subarctic Atlantic are representative of contemporaneous broad-scale changes in planktonic biomass and productivity.

The above back-trajectory and correlation analyses are connected through an empirical orthogonal function (EOF) analysis of satellite NPP, which reveals the leading mode of summertime and annual NPP variability (NPP PC1; around 20% and 24% explained variance, respectively) to be closely aligned with [MSA] PC1 over multiannual timescales (Fig. 3d and Methods), while also remaining notably consistent with spatially integrated summertime and annual NPP yields ($r = 0.75$ and 0.91 , respectively; Extended Data Fig. 2). This latter similarity is underscored (Fig. 3c) by the broadly coherent loading pattern of NPP PC1 (EOF1), which spatially links marine productivity across a broad portion of the Irminger, Labrador and western-Icelandic Seas (Fig. 3c). Notably, the analysis also reveals the extrema of NPP EOF1 to directly overlap with the [MSA] PC1 air mass density maxima and altitude minima (Fig. 2b, c). Given moderate stability in the spatial character of productivity variability during the past (and the underlying phytoplankton assemblages that comprise it), this independently confirms that DMS emissions from this region—once converted to MSA in the atmosphere and deposited atop the GrIS—are suitable for reconstructing broad-scale subarctic Atlantic productivity variations.

Results from our combined back-trajectory (Fig. 2b, c), correlation (Fig. 3b and Extended Data Fig. 7) and EOF (Fig. 3c) analyses support our use of the [MSA] PC1 signal (Fig. 2a) as an index for past variations in marine productivity across the subarctic Atlantic basin. Our ice-core-based productivity index is remarkably consistent with the twentieth century decline in (basin-scale) North Atlantic planktonic stocks that has previously been reported¹¹ ($P < 0.0001$; Extended Data Fig. 8a), as well as broadly congruent with several CPR-based indices of subarctic Atlantic planktonic abundance (Fig. 4a, Methods and Extended Data Fig. 3). Notably, all records show a pronounced decline over the second half of the twentieth century, followed by recent intermittent (probably natural-decadal) variability in productivity that has thus far characterized the contemporary satellite era (Fig. 4a and

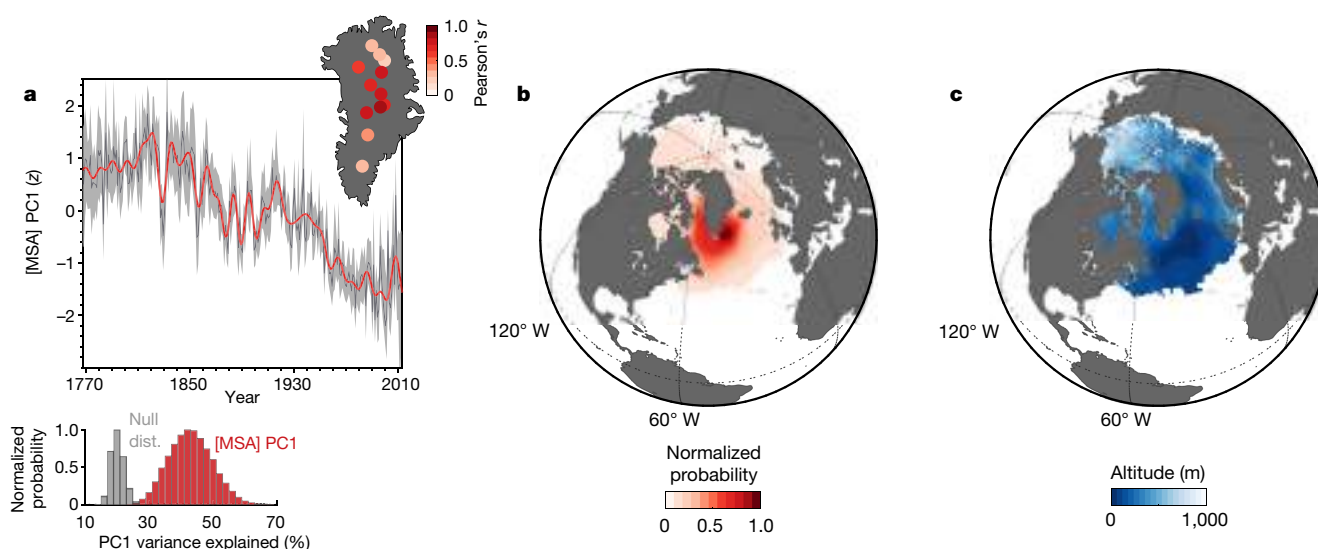


Fig. 2 | [MSA] PC1 and atmospheric back-trajectory modelling of probable MSA source regions. **a**, Top, time series of [MSA] PC1. The black and red lines show the 1-year and 10-year low-pass-filtered resolutions, respectively, with bootstrap-based 95% confidence interval ($n = 10,000$; see Methods). Units (z) denote standard variance. Bottom, normalized probability histogram illustrating the variance explained by [MSA] PC1 following 10,000 bootstrap-sampling principal-component tests (red; Methods). Also shown is the null distribution of PC1-explained variance (grey) following 10,000 principal component analyses conducted upon pseudo-random surrogate [MSA] datasets, revealing the [MSA] PC1 series to be significantly different from noise at the $P = 0.002$ level (one-sided, two-sample Kolmogorov–Smirnov test). The inset map shows

the position of each site on the GrIS and its homogenous correlation with [MSA] PC1 over the period AD 1821–1985 (see Extended Data Table 1 for values). **b**, Site-weighted [MSA] PC1 JJA marine-airmass transport density map—representing the relative probability of an oceanic airmass passing through a given atmospheric column en route to the GrIS (Methods)—normalized on a 0–1 (least to most probable) scale. **c**, Site-weighted [MSA] PC1 median atmospheric altitude for all ocean-situated JJA hourly trajectory locations over the period AD 1948–2013. The primary source of GrIS [MSA] is assumed to overlap with regions representing high airmass transport densities and (or) low median atmospheric altitudes (see also Extended Data Figs. 4, 5).

Extended Data Fig. 2). Moreover, our multi-century productivity record markedly extends prior spatiotemporally limited ship-based observations beyond the mid-twentieth century¹¹, suggesting that the decline seen in the twentieth century is part of a much longer-term trend.

The additional temporal context of our productivity index allows us to investigate subarctic Atlantic productivity responses to changes in atmospheric and oceanic forcing over recent decades, here characterized by indices of the North Atlantic Oscillation^{24,25} (NAO) and Subpolar Gyre (SPG) circulation strength²². Using correlation analysis (Extended Data Fig. 8a and Methods), we find that the NAO is only weakly related to our reconstructed bioproductivity variations, whereas SPG strength shows a significant negative influence over decadal timescales as has previously been shown by sparse ship-based colour data¹⁷. Modelling studies suggest that during weakened^{26,27} and (or) contracted²² SPG states, the wintertime depth of the mixed layer deepens across the central-northeastern subarctic Atlantic and shoals

across the Labrador Sea²⁷. Thus, in addition to its first-order inverse effect on northeastern Atlantic SST variability²² (Fig. 4a), this could explain how a weak SPG, by enhancing wintertime deep-water nutrient replenishment to the euphotic zone^{1,5,9,13}, or by delaying the seasonal onset of predatorial grazing cycles¹⁴ across the ecologically productive central-northeastern Atlantic¹⁷ (Fig. 3a), could lead to the increases in NPP observed in our results.

Differential change-point analysis^{4,16} of our [MSA] PC1 record suggests that the decline in subarctic Atlantic productivity began in AD 1816 ± 11 years (Fig. 4a and Methods), which is broadly consistent with the onset of regional surface temperature warming⁴. Applying

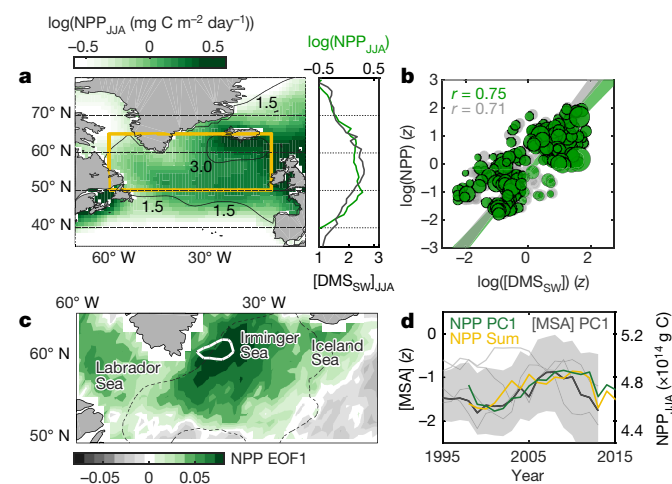


Fig. 3 | Strong agreement between subarctic Atlantic NPP, [DMS_{SW}] and [MSA] PC1. **a**, North Atlantic mean (log-transformed) satellite JJA VGPM NPP rates (Methods; display data smoothed using a $3^\circ \times 3^\circ$ boxcar filter). Black contours show JJA [DMS_{SW}] isopleths (nM) reproduced from a previously published study²³. Right, North Atlantic zonal NPP and [DMS_{SW}] averages. **b**, Weighted (green; $n = 184$ degrees of freedom) and ordinary (grey; $n = 222$ degrees of freedom; Methods) least squares regression analysis of subarctic Atlantic [DMS_{SW}] versus NPP rate; both regressions are significant ($P < 0.0001$), using a two-tailed Student's t -distribution with a t -statistic representing $n - 2$ degrees of freedom. Regression values (r) represent Pearson product-moment coefficients. Shaded bands show the 95% confidence interval of the regression. The diameter of the green circles represents the relative weighting attributed to [DMS_{SW}] (Methods). **c**, Leading EOF (20% of variance explained) of subarctic Atlantic summertime-integrated VGPM NPP yields (AD 1998–2017; 50° – 65° N, 60° – 10° W), showing strong overlap with the 95th-percentile [MSA] PC1 airmass transport density (white bold line; Fig. 2b) and 5th-percentile [MSA] PC1 median trajectory altitude isopleths (black dotted-dashed line; Fig. 2c). **d**, PC1-based projection of summertime VGPM NPP yields (green) alongside the subarctic Atlantic-integrated NPP yield time series (yellow), overlaid by [MSA] PC1 (with grey bootstrap-based 95% confidence interval); all time series are smoothed using a 5-year running mean. Individual (5-year smoothed) [MSA] records that overlap the satellite era are shown for comparison as light-grey lines. The yellow box in **a** indicates the area shown in **c**.

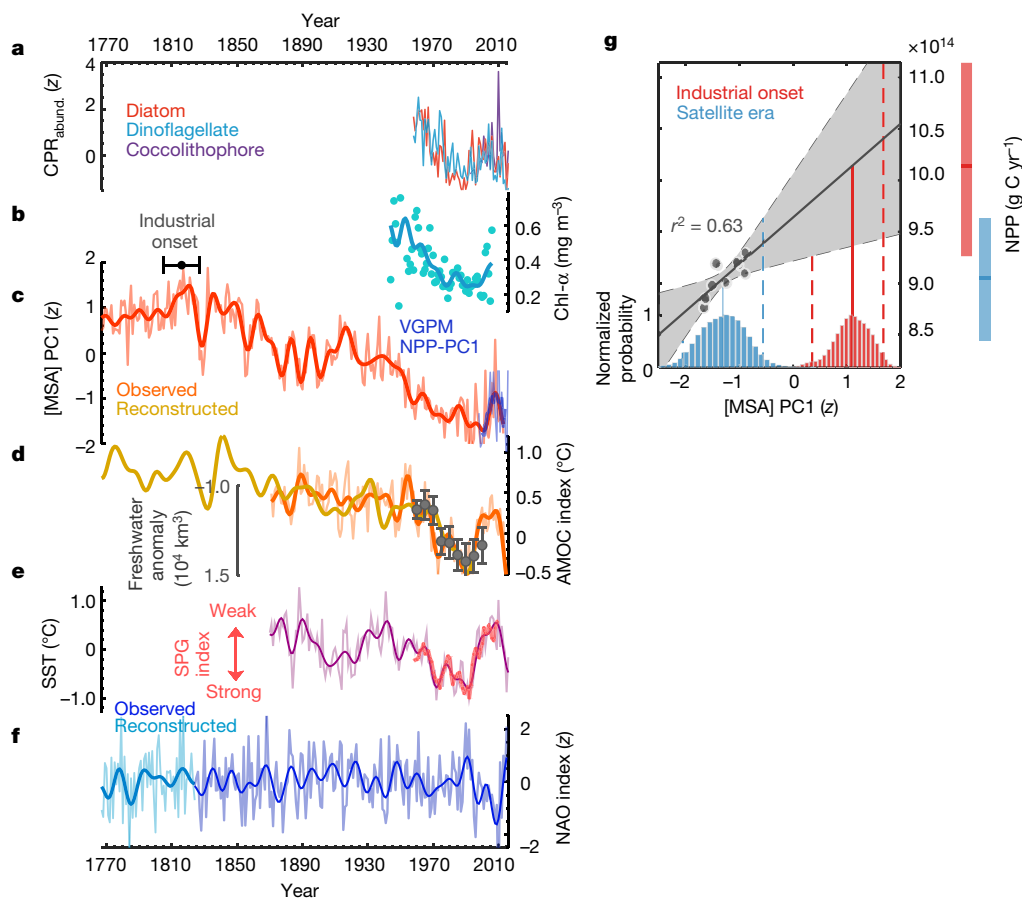


Fig. 4 | Multi-century decline of subarctic Atlantic productivity.

a, Standardized (z -score units relative to AD 1958–2016) indices of Continuous Plankton Recorder (CPR)-based diatom, dinoflagellate and coccolithophore abundances (Methods). **b**, North Atlantic [chlorophyll- α] reconstruction¹¹, limited to the period of annually contiguous data availability (AD 1944–2006). **c**, [MSA] PC1 productivity index and 5-year smoothed NPP PC1 (relative scale; Fig. 3c). The onset range shows the estimated industrial-era initiation (1816 ± 11 years; Methods) of declining productivity. **d**, Reconstructed⁶ and observed⁸ AMOC index and 5-year averaged subarctic Atlantic freshwater storage anomalies²⁸ ($\pm 2\sigma$; anomalies relative to AD 1955). **e**, Subarctic Atlantic warming hole SST anomalies³⁰, mean-centred relative to AD 1870–2016 (Extended Data Fig. 9) and an extended SPG index²² (relative scale; Supplementary Information). **f**, Observed²⁴ and reconstructed²⁵ NAO index. All thin and bold lines show the 1-year and 10-year low-pass-filtered resolution,

a calibration derived from the relationship between [MSA] PC1 and the leading mode of twenty-first century satellite-derived NPP (Fig. 3d and Extended Data Fig. 2), we calculate an estimated $10 \pm 7\%$ decline (mean $\pm 2\sigma$; Fig. 4b) in contemporary subarctic Atlantic NPP yields since the onset of the industrial era. Despite the uncertainties of this estimate, arising from the short time span of satellite-derived NPP estimation (Fig. 4a) and limited availability of GrIS [MSA] data during this period (Fig. 3d and Methods), the onset of declining subarctic Atlantic productivity appears temporally consistent with the (approximately 15%) decline in industrial-era Atlantic thermohaline overturning strength (that is, AMOC) that has recently been inferred from marine sediments in the Labrador and Irminger basins⁸. We similarly observe strong multidecadal to centennial scale correspondence ($P < 0.0001$) between our productivity index and a separate, high-resolution terrestrial proxy-based reconstruction⁶ of AMOC based on northeastern Atlantic upper-ocean heating anomalies (Fig. 4a, Extended Data Fig. 9 and Supplementary Information). These results, which suggest a positive relationship between productivity, subarctic Atlantic SSTs and large-scale thermohaline variability across decadal-scale and longer timescales, contrast model-based contentions

respectively, unless otherwise noted. **g**, Weighted least squares calibration of 5-year smoothed [MSA] PC1 and NPP PC1 ($n = 12$ years; $r^2 = 0.63$; $P = 0.07$ after adjusting for reduced degrees of freedom; Methods). The regression weights are the inverse standard deviation of [MSA] PC1 values (see also Fig. 3d). Blue and red distributions show the range of industrial-era onset and satellite-era [MSA] PC1 values following 10,000 bootstrap tests (both distributions are normalized to their respective modes, with bold and dashed vertical lines denoting the 50th and 2.5–97.5th percentiles, respectively). The grey-shaded region shows the 95% confidence interval of the regression parameters. The corresponding 95% confidence ranges of industrial-era onset and satellite-era annual NPP yields are projected as vertical bands to the right, suggesting a mean decline of approximately $10 \pm 7\%$ NPP (mean $\pm 2\sigma$) over the industrial era.

of a positive (that is, reinforcing) influence of SPG-circulation strength on both subarctic Atlantic overturning²⁶ and, by extension, productivity.

The strong observed coherence between productivity and AMOC strength, moreover, supports a previous model-based hypothesis⁵ that a sustained, industrial-era slowdown of AMOC^{6–8} would lead to markedly reduced planktonic yields across the northern Atlantic. In particular, both [MSA] PC1 and AMOC exhibit corresponding multi-century-scale^{6,8} lows during the 1980s to 1990s. This time period coincides with a massive accumulation of freshwater (around $15,000 \text{ km}^3$ from 1965 to 1990) into the subarctic Atlantic basin following the great salinity anomaly²⁸ of the late 1960s (Fig. 4a). According to the relationships that we found, the decrease in upper-ocean densities associated with this event, which has been hypothesized to have weakened deep-water formation across the Labrador and Irminger Seas^{6,28}, may also have led to a diminishing of northern Atlantic planktonic stocks, presumably either through long-term shoaling of the wintertime depth of the mixed layer and the gradual diminishing of euphotic nutrient concentrations^{1,5,9}, or through first-order thermal influences^{1,12}. Furthermore, the onset of industrial-era declines in Arctic sea ice

and elevated GrIS runoff, which started several decades after our productivity decline and are currently accelerating^{15,16}, suggests that a long-term influx of fresh water into (that is, a freshening of) northeastern subarctic Atlantic surface waters—similarly implicated in driving the industrial-era AMOC decline^{1,6–8}—may have contributed in sustaining the industrial-era productivity decline over the late nineteenth and twentieth centuries. However, more work is needed to understand these complex relationships.

Our ice-core-based index of subarctic Atlantic bioproductivity highlights the sensitivity of marine-based autotrophic ecosystems to industrial-era forcing and provides context for projected future ecological changes⁶. Although previous ship-based^{11,17} and satellite-derived reconstructions suggested an early twenty-first century reversal in the twentieth century decline in subarctic Atlantic productivity (Fig. 4a), results from our [MSA] PC1 proxy show that the decline on which this intermittent twenty-first century increase is superimposed is much longer than previously observed¹¹ and may still be ongoing. Monitoring of the AMOC at 26.5° N since 2004 has shown a decade-long decline in meridional heat transport, decreasing as much as 10 times faster than model-predicted slowdowns²⁹. Given the multiyear time lag required of Atlantic-wide mixing^{13,22}, as well as the ongoing, nonlinear rise in Greenland runoff¹⁶ believed to contribute to subarctic Atlantic freshening and AMOC slowdown over multidecadal to centennial timescales^{6,8,10}, we speculate that declining subarctic Atlantic productivity will characterize the coming decades with important implications for future atmospheric carbon drawdown³ and northern Atlantic fisheries².

Online content

Any methods, additional references, Nature Research reporting summaries, source data, statements of data availability and associated accession codes are available at <https://doi.org/10.1038/s41586-019-1181-8>.

Received: 1 October 2018; Accepted: 8 April 2019;

Published online: 20 May 2019

- Barton, A. D., Irwin, A. J., Finkel, Z. V. & Stock, C. A. Anthropogenic climate change drives shift and shuffle in North Atlantic phytoplankton communities. *Proc. Natl Acad. Sci. USA* **113**, 2964–2969 (2016).
- Stock, C. A. et al. Reconciling fisheries catch and ocean productivity. *Proc. Natl Acad. Sci. USA* **114**, E1441–E1449 (2017).
- Takahashi, T. et al. Climatological mean and decadal change in surface ocean pCO₂, and net sea-air CO₂ flux over the global oceans. *Deep. Res. II* **56**, 554–577 (2009).
- Abram, N. J. et al. Early onset of industrial-era warming across the oceans and continents. *Nature* **536**, 411–418 (2016).
- Schmittner, A. Decline of the marine ecosystem caused by a reduction in the Atlantic overturning circulation. *Nature* **434**, 628–633 (2005).
- Rahmstorf, S. et al. Exceptional twentieth-century slowdown in Atlantic Ocean overturning circulation. *Nat. Clim. Change* **5**, 475–480 (2015).
- Caesar, L., Rahmstorf, S., Robinson, A., Feulner, G. & Saba, V. Observed fingerprint of a weakening Atlantic Ocean overturning circulation. *Nature* **556**, 191–196 (2018).
- Thornalley, D. J. R. et al. Anomalously weak Labrador Sea convection and Atlantic overturning during the past 150 years. *Nature* **556**, 227–230 (2018).
- Moore, J. K. et al. Sustained climate warming drives declining marine biological productivity. *Science* **359**, 1139–1143 (2018).
- Bakker, P. et al. Fate of the Atlantic Meridional Overturning Circulation: strong decline under continued warming and Greenland melting. *Geophys. Res. Lett.* **43**, 12252–12260 (2016).
- Boyce, D. G., Lewis, M. R. & Worm, B. Global phytoplankton decline over the past century. *Nature* **466**, 591–596 (2010).
- Behrenfeld, M. J. & Falkowski, P. G. Photosynthetic rates derived from satellite-based chlorophyll concentration. *Limnol. Oceanogr.* **42**, 1–20 (1997).
- Sverdrup, H. U. On conditions for the vernal blooming of phytoplankton. *ICES J. Mar. Sci.* **18**, 287–295 (1953).
- Behrenfeld, M. J. & Boss, E. S. Resurrecting the ecological underpinnings of ocean plankton blooms. *Annu. Rev. Mar. Sci.* **6**, 167–194 (2014).
- Kinnard, C. et al. Reconstructed changes in Arctic sea ice over the past 1,450 years. *Nature* **479**, 509–512 (2011).
- Trusel, L. D. et al. Nonlinear rise in Greenland runoff in response to post-industrial Arctic warming. *Nature* **564**, 104–108 (2018).
- Hátún, H. et al. Large bio-geographical shifts in the north-eastern Atlantic Ocean: from the subpolar gyre, via plankton, to blue whiting and pilot whales. *Prog. Oceanogr.* **80**, 149–162 (2009).
- Legrand, M. et al. Sulfur-containing species (methanesulfonate and SO₄) over the last climatic cycle in the Greenland Ice Core Project (central Greenland) ice core. *J. Geophys. Res.* **102**, 26663–26679 (1997).
- Stefels, J., Steinke, M., Turner, S., Malin, G. & Belviso, S. Environmental constraints on the production and removal of the climatically active gas dimethylsulphide (DMS) and implications for ecosystem modelling. *Biogeochemistry* **83**, 245–275 (2007).
- Charlson, R. J., Lovelock, J. E., Andreae, M. O. & Warren, S. G. Oceanic phytoplankton, atmospheric sulphur, cloud albedo and climate. *Nature* **326**, 655–661 (1987).
- Polashenski, D. J. et al. Denali ice core methanesulfonic acid records North Pacific marine primary production. *J. Geophys. Res.* **123**, 4642–4653 (2018).
- Hátún, H., Sandø, A. B., Drange, H., Hansen, B. & Valdimarsson, H. Influence of the Atlantic subpolar gyre on the thermohaline circulation. *Science* **309**, 1841–1844 (2005).
- Lana, A. et al. An updated climatology of surface dimethylsulfide concentrations and emission fluxes in the global ocean. *Glob. Biogeochem. Cycles* **25**, GB1004 (2011).
- Jones, P. D., Jónsson, T. & Wheeler, D. Extension to the North Atlantic Oscillation using early instrumental pressure observations from Gibraltar and South-West Iceland. *Int. J. Climatol.* **17**, 1433–1450 (1997).
- Ortega, P. et al. A model-tested North Atlantic Oscillation reconstruction for the past millennium. *Nature* **523**, 71–74 (2015).
- Sgubin, G., Swingedouw, D., Drijfhout, S., Mary, Y. & Bennabi, A. Abrupt cooling over the North Atlantic in modern climate models. *Nat. Commun.* **8**, 14375 (2017).
- Born, A. et al. Is the Atlantic subpolar gyre bistable in comprehensive coupled climate models? *Clim. Dyn.* **40**, 2993–3007 (2013).
- Curry, R. & Mauritzen, C. Dilution of the northern North Atlantic Ocean in recent decades. *Science* **308**, 1772–1774 (2005).
- Srokosz, M. A. & Bryden, H. L. Observing the Atlantic Meridional Overturning Circulation yields a decade of inevitable surprises. *Science* **348**, 1255575 (2015).
- Huang, B. et al. Extended reconstructed sea surface temperature, version 5 (ERSSTv5): upgrades, validations, and intercomparisons. *J. Clim.* **30**, 8179–8205 (2017).

Acknowledgements We thank D. Thornalley, R. Ji and Ø. Paasche for their feedback on early versions of the study, as well as H. Hátún, D. G. Boyce and D. Johns for contributing oceanographic and planktonic data shown in the study; M. Legrand for sharing the GRIP93a ice core [MSA] data; the students and staff of the DRI ice core group for assistance in the field and laboratory; the National Science Foundation (NSF) Ice Core Facility (formerly NICL), A. York, M. Bingham, M. Hatch and Milton Academy students for the Greenland Central (GC) ice core sampling, processing and [MSA] analysis support. Funding for retrieval and analysis of the GC ice core was provided by the US NSF Arctic System Science Program (award OPP-1205196 to S.B.D. and OPP-1205008 to M.J.E.). M.B.O. acknowledges support from the US Department of Defense Office of Naval Research – National Defense Science and Engineering Graduate (NDSEG) fellowship, and an Ocean Outlook Fellowship to the Bjerknes Centre for Climate Research. M.B.O. and S.B.D. further acknowledge institutional support from the Woods Hole Oceanographic Institution (WHOI). H.F. acknowledges support of the tracer glaciological work along the North Greenland Traverse (NGT) 1993–95 by the German Research Foundation (DFG) and the long-term support of ice core science at the University of Bern by the Swiss National Science Foundation (SNF). Collection and analysis of the D4, TUNU and Summit2010 cores were supported by NSF grants 0221515, 0909541 and 1204176 to J.R.M. E.S.S. acknowledges NASA grant NNX15AF31G.

Reviewer information Nature thanks John Dunne, Rafael Simo and the other anonymous reviewer(s) for their contribution to the peer review of this work.

Author contributions M.B.O. conceived and designed the study with input from S.B.D., S.B.D., M.B.O. and L.D.T. collected the Greenland Central (GC) ice core. M.J.E. analysed the GC ice core chemistry. H.F. and S.K. led the collection and chemical analyses of all five NGT records. M.M.G., J.R.M. and E.S.S. jointly conducted the D4 and TUNU chemical analyses. J.R.M. and E.S.S. analysed the Summit2010 and 20D ice core chemistry, respectively. Data analysis and interpretation were performed by M.B.O., who wrote the manuscript with input from S.B.D. and L.D.T. All authors read and commented on the manuscript.

Competing interests The authors declare no competing interests.

Additional information

Extended data is available for this paper at <https://doi.org/10.1038/s41586-019-1181-8>.

Supplementary information is available for this paper at <https://doi.org/10.1038/s41586-019-1181-8>.

Reprints and permissions information is available at <http://www.nature.com/reprints>.

Correspondence and requests for materials should be addressed to M.B.O.

Publisher's note: Springer Nature remains neutral with regard to jurisdictional claims in published maps and institutional affiliations.

© The Author(s), under exclusive licence to Springer Nature Limited 2019

METHODS

Data reporting. No statistical methods were used to predetermine sample size. The experiments were not randomized.

[MSA] record collection, analysis and preprocessing. Twelve MSA ($\text{CH}_3\text{SO}_3\text{H}$) concentration ([MSA]) ice core records were compiled from sites situated on the GrIS ($n = 12$ records). MSA is measured at trace concentrations in polar ice using its constituent anion, methanesulfonate^{31,32} (CH_3SO_3^-). The five previously published [MSA] records used in this compilation were measured using either conventional ion-chromatography (IC) techniques (20D³¹, NGRIP³³ and GRIP93a¹⁸) or electrospray ionization with triple quadrupole mass spectrometry (Summit2010 and TUNU)³⁴. Specific details on the measurement techniques can be found in the original studies (Extended Data Table 1). Six out of seven of the remaining (previously unpublished) [MSA] records were measured using ion chromatography. Measurement of methanesulfonate in the Greenland Central (GC) record¹⁶ was conducted at Wheaton College with analytical and core-sampling procedures identical to those described previously³⁵. Records derived from the Northern Greenland Traverse (NGT-B16, NGT-B18, NGT-B20, NGT-B21 and NGT-B26) were analysed at the Alfred-Wegener-Institute following the previously published methodology³⁶. The remaining unpublished [MSA] record, D4, was also analysed using electrospray ionization with triple quadrupole mass spectrometry at the Desert Research Institute following previously published methods³⁴.

Records were selected using the following criteria. The records must be of moderate to high temporal resolution (measured at ≤ 3 years per sample; note 10/12 records exist at ≤ 1 year resolution; Fig. 1a), be well-dated (< 5 year estimated uncertainty at the deepest portions of the records presented) and represent > 100 years of continuous length within the period AD 1767–2013. Aspects of all ice cores have been previously published, such that information on the dating methodology of each ice core can be found within references listed in Extended Data Table 1. Before analysis of the [MSA] records, each was linearly interpolated to a resolution of one year. The period of common overlap for all 12 records is AD 1821–1985. It is assumed that dating uncertainties among records are approximately normally distributed, such that dating inconsistencies are effectively averaged out during dimensional reduction. Similarly, although interior Greenlandic ice core [MSA] records are known to experience post-depositional vertical migration, migration directionality is not systematic and may occur in either the (atmosphere-oriented) up or down direction depending primarily on local cationic soluble impurity concentration gradients³⁷. As such, we assume that potential migration-based ‘skewing’ of the original [MSA] signal is largely minimized during data reduction. Finally, although contentions of post-depositional volatile losses of MSA have been reported at high-acidity and low accumulation sites in Antarctica (nominally, $< 100 \text{ kg m}^{-2} \text{ year}^{-1}$)³⁸, such losses are likely largely inhibited across the GrIS, where relatively high accumulation rates, as well as low acidity summer-time layers, prevail (Extended Data Table 1).

Note that a decision was made not to analyse MSA fluxes. This was primarily because of a lack of high-resolution accumulation data for all 12 sites. However, recent century-scale reconstructions of the GrIS accumulation rate, derived from both inland^{39,40} and near-coastal⁴¹ ice cores, do not generally support evidence for spatiotemporally synchronous shifts in accumulation across Greenland nor, to our knowledge, the regional multi-century accumulation increases that are necessary to promote (by dilution) the multi-century decreases in the [MSA] records presented here. Similarly, although MSA is highly hygroscopic and thus generally believed to be primarily wet-deposited on the GrIS³¹, owing to the lack of high-resolution accumulation data, we are prevented from quantitatively discerning the precise partitioning of [MSA] between wet and dry deposition at most (11/12, void 20D) sites. Nonetheless, our necessary assumption of negligible long-term changes in MSA depositional partitioning when spatially averaged across the GrIS appears valid, given—in particular—the strong temporal covariation in [MSA] across differing GrIS moisture source regions (Extended Data Fig. 6 and Extended Data Table 1).

Extraction of [MSA] PC1 and uncertainty estimation. We used an EOF-based data-infilling routine⁴² to infill missing values in the [MSA] records before signal extraction. In our study, missing values occurred at the extremities of the records, and thus represent records that either were collected before AD 2013 or did not extend as deep as AD 1767. Under the criterion that the oldest PC1 age (that is, AD 1767) represents the oldest age for which $> 75\%$ of Greenlandic [MSA] records remain, $< 8\%$ of data points among the 12 records required infilling. For the more recent portion of the PC1 series, we relaxed our 75% record-retention criterion to enable greater temporal overlap with satellite observations (around 1998). Although this relaxation did—in general—invoke a trade-off with declining precision in the [MSA] signal extraction for satellite-interval years (as encapsulated by slightly enlarged widths of the [MSA] PC1 confidence intervals; Figs. 2a, 3d), we nonetheless expect our PC1 extraction to be robust given the strong satellite-era coverage of the Summit2010 record, the largest variance contributor to [MSA] PC1 (Extended Data Table 1).

The EOF-based data-infilling procedure⁴² accounts for covariability between, as well as autocovariance within, individual MSA records, such that strong covariability between two records during a period of common overlap should result in imputed values of comparable covariance between the two records, should one of the records require infilling during a time period for which data exists in the other. Similarly, the autocovariance structure of imputed values within that record should jointly reflect the autocovariance of the measured (that is, non-missing) values of that record. The data-infilling procedure⁴² was conducted as follows: all records were standardized to unit variance and centred to mean zero over their period of common overlap, AD 1821–1985. Missing values were set to zero (an unbiased *a priori* value) and the resultant matrix decomposed into left (temporal EOFs) and right (spatial EOFs) singular vectors using the method of singular value decomposition. The missing (zero) values were then recovered by replacing the zero values with infilled values of the reconstructed [MSA] data matrix, following truncation of both EOF vector spaces. The number of EOFs retained for data infilling was obtained using a Monte Carlo cross-validation approach, in which 5% of the [MSA] data points were withheld at random and iteratively reconstructed with a progressively less-truncated EOF vector space until a specified convergence criterion was met⁴² (root mean square error of prediction (RMSE) $< 10^{-8}$).

We tested the sensitivity of the cross-validation procedure across a large number of data-infilling procedures using the [MSA] Greenlandic array and found that EOF-based data infilling⁴² routinely and robustly reproduced much of the low-frequency variance of the [MSA] dataset across separate tests. However, slight variations in the magnitude of imputed values could occur between tests, an expected result due to the finite size of the [MSA] dataset used for cross-validation. More specifically, variations in the optimal number of EOFs retained for the imputation of missing values could lead to small differences in the fraction of the original variance restored in the imputed [MSA] values between tests. In our case, the number of retained EOFs varied most often between 2 and 4, representing around 50–65% of the [MSA] variance. Because the amount of variance restored back into the imputed data will always be less than the original data, a method was required to restore the remaining variance. To do so, we adopted an approach similar to a previously described method¹⁵, in which—for each test—we divided the infilled [MSA] data matrix into signal and noise components. The signal represents the retained [MSA] data matrix, constructed by applying the inverse EOF transform to the [MSA] dataset using only as many EOFs as were determined to optimally construct the imputed values. Conversely, the noise represents the residual [MSA] data matrix constructed by applying the inverse EOF transform with the remaining EOFs. We applied the method of Cholesky factorization to the noise component of each record, in order to produce pseudo-random noise vectors—that is, randomized vectors with autocorrelation identical to the noise component of each record—that could be added back to the imputed values in sequence and restore variance to the solution. In practice, our pseudo-random variance-restoration routine encourages enlarged uncertainty attribution in portions of the [MSA] PC1 record that required data infilling (that is, the extremities of the dataset; see Figs. 2a, 3d).

We incorporated a probabilistic principal component analysis in order to reduce noise among the 12 [MSA] records and better extract a meaningful mode of common variability, as well as to provide insight into the spatial distribution of homogenous [MSA] signals across the GrIS (Fig. 1c, Extended Data Fig. 3 and Supplementary Information). Extraction of the Greenlandic [MSA] PC1 signal, including estimation of its confidence intervals, was conducted using the following procedure. First, the [MSA] dataset, X_i , was centred to mean zero and standardized to unit variance, with missing values in X_i set to 0. Second, missing values in X_i were statistically infilled following a previously published method⁴², with pseudo-random variance restoration in the imputed values enforced. Third, this second step was repeated for an additional 99 realizations ($n = 100$ realizations total), with each $X_j = X_1, X_2, \dots, X_n$ stored for later use. Fourth, for each $i = 1, 2, \dots, n$ imputed [MSA] datasets, $j = 1, 2, \dots, n$ surrogate [MSA] datasets of equal dimension were created using uniform-random sampling with replacement of the [MSA] records (that is, a bootstrap approach)⁴³. Fifth, principal component analysis was performed on each $X_{i,j}$ ($n^2 = 10^4$) surrogate [MSA] dataset, transformed using orthogonal Procrustes rotation in order to correct for (Eigen-transform) rotational ambiguity⁴³ and the PC1 was extracted and stored. Finally, the confidence intervals were computed using the 2.5–97.5th percentiles of the PC1 distribution (representing all n^2 tests). The ‘best-fit’ PC1 signal represents the median fit (50th percentile) of the distribution. For a comparison with alternate methods of missing data estimation and [MSA] PC1 extraction, see Supplementary Information.

Attribution of probable MSA source regions. Changes in atmospheric circulation and windiness can affect aerosol transport and deposition across the GrIS, affecting the fidelity of ice core climate records across various timescales^{32–34,44–49}. Heterogeneous signals existing across our 12 GrIS [MSA] records, owing to localized productivity and (or) atmospheric variations that are particularly salient across interannual to subdecadal timescales^{44–46}, are largely suppressed by

dimensional reduction of the 12 [MSA] records into [MSA] PC1 and through multi-tear smoothing of the PC1 series thereafter (Fig. 2a and Extended Data Fig. 6).

Over longer, multidecadal to centennial timescales, current evidence^{25,26} does not generally support significant shifts in recent internally driven, regional lower-atmospheric dynamics, suggesting that the primary emission source should underlie the most probable (mean state) trajectory pathway taken by low-lying Greenland-bound air parcels when integrated across several decades (see also Supplementary Information). To support this latter suggestion, we used the National Oceanic and Atmospheric Administration (NOAA) Air Resources Laboratory's hybrid single-particle Lagrangian integrated trajectory (HYSPLIT) model, version 4.9⁵⁰ to enable estimates of probable marine source regions of MSA at each site. HYSPLIT uses a joint Lagrangian–Eulerian approach, in which numerical singularities, or atmospheric ‘particles’, are subjected to a time-variant, spatially fixed three-dimensional gridded wind field across a time-invariant land-surface field and tracked backwards in time at hourly time steps.

Particle trajectories were forced using atmospheric wind data from the National Centers for Environmental Protection and Atmospheric Research (NCEP/NCAR) global atmospheric reanalysis dataset⁵¹, gridded at $2.5^\circ \times 2.5^\circ$ resolution over 17 pressure levels (1,000, 925, 850, 700, 600, 500, 400, 300, 250, 200, 150, 100, 70, 50, 30, 20 and 10 hPa). The HYSPLIT model forced using the NCEP/NCAR wind reanalysis has been shown to provide comparable results to HYSPLIT trajectories forced using higher-resolution (for example, 1° -gridded) wind reanalysis products from the European centre for medium-range weather forecasts⁴⁴.

Because position errors of an individual air mass back trajectory are estimated to upwards of 30% of distance travelled^{45,46}, a probabilistic approach was taken here, in which a large number of trajectories were computed and integrated into airmass transport density maps. In order to focus on low elevation air masses (around 0–1,000 m), which are assumed to be more representative of regional marine-derived moisture and aerosol sources, all particle back trajectories were initialized from a height of 500 m above ground level and released daily during the months June–July–August from AD 1948 to 2013. In total, 6,121 trajectories were released above each ice core site (that is, 73,452 total) and tracked hourly for 7 days before the particle release date, coinciding with the approximate atmospheric lifetime of MSA⁴⁶. At the end of each model trajectory simulation, all hourly trajectory locations situated over the ocean were summed in discrete $1^\circ \times 1^\circ$ bins and area-normalized to produce the marine-airmass transport density grids, nominally representing the relative probability that any given trajectory end-point would be situated over a given grid cell at any point along a trajectory. Owing to the inherent concentric partitioning of trajectory end-points around the trajectory release point, each grid cell within the transport density grid was then normalized by its inverse radial distance from the trajectory release point to remove its central tendency⁴⁹. Finally, all airmass transport density grids were normalized on a 0–1 (least to most probable) relative scale. In addition, the median particle trajectory height for each grid box was computed to target regions that consisted of predominantly low-lying oceanic airmasses and thus those originating within the marine boundary layer.

In order to achieve an airmass transport density (and median atmospheric elevation) grid statistically representative of the [MSA] PC1 series, we composited the airmass transport density grids (and median atmospheric elevation grids) of the 12 sites into a single map. This was achieved by weighting the 12 individual airmass transport density grids (and median atmospheric elevation grids) by the squared correlation of each site (that is, the fraction of variance shared) with the [MSA] PC1 signal over the common-overlap period AD 1821–1985 (Extended Data Table 1) before compositing. Note that the inferred source region, situated over the central-northeast subarctic Atlantic in the vicinity of the Irminger and Icelandic Basins (Fig. 2c, d), is also considerably removed from the summertime sea ice marginal front where GrIS-deposited MSA origination has previously been attributed³⁴. For a more in-depth analysis of the possible maritime source regions of Greenlandic MSA on a per-site basis, see Supplementary Information (see also Extended Data Figs. 4, 5).

Correlation analysis of subarctic Atlantic [DMS_{SW}] measurements to satellite NPP. We compared surface [DMS_{SW}] to satellite-derived NPP estimates (Fig. 2b) using measurements of [DMS_{SW}] compiled within the NOAA Global Surface Seawater DMS Database^{23,52} for the period 1 January 1998 to 31 December 2016. This period was chosen in order to overlap with ocean colour measurements from leading satellite sensors (for example, SeaWiFS, late 1997–2009, and MODIS-AQUA, mid 2002–present; Supplementary Information). It is important to note that no quality control on the [DMS_{SW}] measurements compiled in the database currently exists, due to the lack of [DMS_{SW}] measurement protocols, or inter-calibration methodologies²³. Rather, in order to remove anomalous [DMS_{SW}] values, measurements that represent the middle 95% of concentrations were retained for analysis. This resulted in 30,047 measurements. As [DMS_{SW}] values archived within the database are most often clustered in space and time, values were binned monthly at $1^\circ \times 1^\circ$ -gridded resolution, log-transformed to achieve normality and heteroscedasticity and averaged. This procedure resulted in

a reduction from 30,047 global measurements to 3,045 unique global data points, a much smaller subset of which ($n = 224$) derives from the subarctic Atlantic (50° – 65° N; 60° – 10° W). We then upsampled (using two-dimensional linear interpolation) the $1/6^\circ \times 1/6^\circ$ -gridded estimates of log-transformed ocean NPP, taken from the VGPM¹², onto a centred $1^\circ \times 1^\circ$ spatial grid. All unique [DMS_{SW}] data points were regressed against the corresponding (log-transformed and standardized) NPP $1^\circ \times 1^\circ \times 1$ -month grid point using ordinary least squares. For [DMS_{SW}] grid points in the subarctic Atlantic with more than one observation ($n = 186$ out of 224 total measurements), linear regression analysis was conducted using weighted least squares (WLS; where weights represent the inverse standard error of each average [DMS_{SW}] value measured within a given $1^\circ \times 1^\circ \times 1$ -month bin) against the corresponding NPP value. An analysis of the relationship between global versus subarctic Atlantic [DMS_{SW}] and NPP can be found in Extended Data Fig. 7 (see also Supplementary Information).

Processing of continuous phytoplankton recorder survey data. For inferences of subarctic Atlantic phytoplankton abundance changes that have occurred since the mid-twentieth century, we use data from the Continuous Phytoplankton Recorder (CPR) survey. As reviewed previously⁵³, the CPR remains the most extensive (in spatial scale, taxonomic scope and time period covered) independent ocean-biological monitoring program in current existence, having recorded the abundance of nearly 700 unique taxa since AD 1931. The sampling methodology consists of towing a filtering device at approximately 10-m depth along standard shipping routes using ships of opportunity; each sample corresponds to 10 nautical miles (approximately 18 km) or around 3 m^3 of filtered water. Phytoplankton are collected on a $270\text{-}\mu\text{m}$ mesh, a size originally chosen to provide broad representation of planktonic species, including both larger predatorial functional groups (for example, copepods, pteropods and small crustaceans) and large-diameter autotrophic phytoplankton. Despite this mesh size, smaller planktonic species—including coccolithophores (approximately $10\text{-}\mu\text{m}$) and diatoms (around $10\text{--}200\text{-}\mu\text{m}$)—are also consistently captured on the silk mesh and recorded for abundance. Notably, because the sampling methodology has remained relatively unchanged since the inception of the survey, consistency of planktonic time series has been correspondingly maintained and relative changes in planktonic abundance are considered to be generally robust irrespective of size and (or) functional group⁵³. On the other hand, given the host of complicating factors that pertain to the collection and counting of differently sized microorganisms in a given measurement (for example, planktonic active avoidance or escape, mesh-clogging, cell visibility)⁵³, as well as the associated challenge therein of converting relative abundance measurements to absolute abundance, CPR measurements must nonetheless be cautioned as semi-quantitative by nature.

Here we assess CPR products of monthly total diatom (1958–2016), dinoflagellate (1958–2016) and coccolithophore (1993–2016) abundances within pre-existing CPR standard regions situated over the subarctic Atlantic (that is, 50° – 65° N, 60° – 10° W, 14/41 CPR standard regions: A6, A8, B5–B8, C5–C8 and D5–D8; see Extended Data Fig. 3 and a previously published study⁵³). We included coccolithophore, dinoflagellate and diatom relative abundances, as these functional groups share both a known association to DMS production¹⁹ and, collectively, are believed to comprise the bulk of abundance of autotrophic biomass in the subarctic Atlantic regions^{17,53}. Towards this latter point, the decision to analyse each group was also of pragmatic intent, as each provided adequate CPR spatiotemporal coverage in most of the subarctic Atlantic regions over recent decades⁵³ (Extended Data Fig. 3). Conversely, because larger-diameter heterotrophs, such as copepods and other zooplankton, are not directly linked to DMS production (voiding their indirect association via sloppy grazing and excretion¹⁹) and furthermore raise additional issues of systematic sampling bias due to, for example, CPR inlet active avoidance and escape⁵³, we did not directly consider these higher-order functional groups within our assessments¹⁷.

As noted previously⁵³, a potential bias in decadal time series of CPR data arises from the gradual increase in Atlantic shipping speeds since the mid-twentieth century. This shipping-speed increase is believed to have had a systematic, and near-linear, negative effect on the amount of water filtered through CPR devices, thus (negatively) biasing long-term relative abundance trends⁵⁴. As such, we correct for this potential bias using conservative (that is, extreme case) empirical relationships that have been established previously⁵⁴ between increasing mean northeastern-Atlantic shipping-speed trends ($0.09 \text{ knots year}^{-1}$ since 1958) and volume of water filtered ($-0.26 \text{ m}^3 \text{ knot}^{-1}$; all corrections made relative to a mean filtered-water volume of 3.16 m^3 in AD 1990). As shown in Extended Data Fig. 3c, d, this ship-speed bias adjustment imparts only minor adjustments to the ‘raw’ CPR abundance data over the considered time period.

WLS regressions of CPR abundance against [DMS_{SW}] (Extended Data Fig. 7) were conducted following the procedure described for [DMS_{SW}] versus NPP (see above), the primary difference being that monthly [DMS_{SW}] values were instead averaged within entire CPR standard regions (as opposed to degree latitude–longitude bins) before regression. Relationships between [DMS_{SW}] and

CPR abundance were not found to be significantly different when using either the ship-speed bias-adjusted or raw CPR data (Extended Data Fig. 3).

Time series of annual subarctic Atlantic phytoplankton abundance (shown in Fig. 4a) were estimated by first calculating annual means in each CPR standard region containing ≥ 8 months of data (Supplementary Information). We report CPR time series as the simple area-weighted average of the CPR abundance data for each standard region across the subarctic Atlantic (which vary substantially in size). A comparison of subarctic Atlantic CPR time series—for both summertime- and annual-based measurements—to alternative probabilistic and deterministic data infilling and compositing techniques that better account for regional-sampling biases is provided in Extended Data Fig. 3 (see also Supplementary Information for an extended discussion).

Time series statistical significance testing. Statistical significance levels for all reported time series correlations (Pearson's r in all instances) were computed using a nonparametric Monte Carlo-based method⁵⁵, unless noted otherwise. We created $n = 10,000$ pseudo-random surrogate series of the first series by computing its Fourier transform, randomly varying the phase of its Fourier modes between 0 and 2π , and then computing the inverse transform, thus retaining the exact autocorrelative properties (that is, power spectrum preservation) of the original series. Statistical significance was then estimated by computing n pseudo-random correlations with the original second series and by calculating the exceedance probability (that is, inverse percentile) of achieving a correlation magnitude greater than the original by chance alone. Note that the maximum degree of significance that can be achieved using this method is $P < n^{-1}$, such that a value reported as $P < 0.0001$ represents an observed correlation magnitude greater than all n pseudo-random correlations (Extended Data Table 1).

Productivity-decline onset timing. The onset timing of the industrial-era productivity decline was estimated using the SiZer (significant zero crossings of derivatives) methodology⁵⁶, conducted in a manner similar to the previously described methods^{14,16}. In brief, we calculated the median significant ($P < 0.1$) onset of sustained (that is, requiring the sign of the trend to persist into the present) [MSA] PC1 decline following prefiltering of the series across a range of Gaussian kernel filters. We assessed 26 filters incrementally distributed with 15–40-year bandwidths. To alleviate edge-effect biases stemming from our comparably short^{14,16} time series, we mandated each productivity-decline onset age to be at least one filter-width greater (that is, more recent than) the oldest age of our time series (that is, AD 1767). As such, our estimated industrial-era productivity-decline onset, AD 1816 ± 11 years (± 2 median absolute deviations), represents the SiZer solution using a smaller subset (14/26) of the originally filtered [MSA] PC1 series.

Reporting summary. Further information on research design is available in the Nature Research Reporting Summary linked to this paper.

Data availability

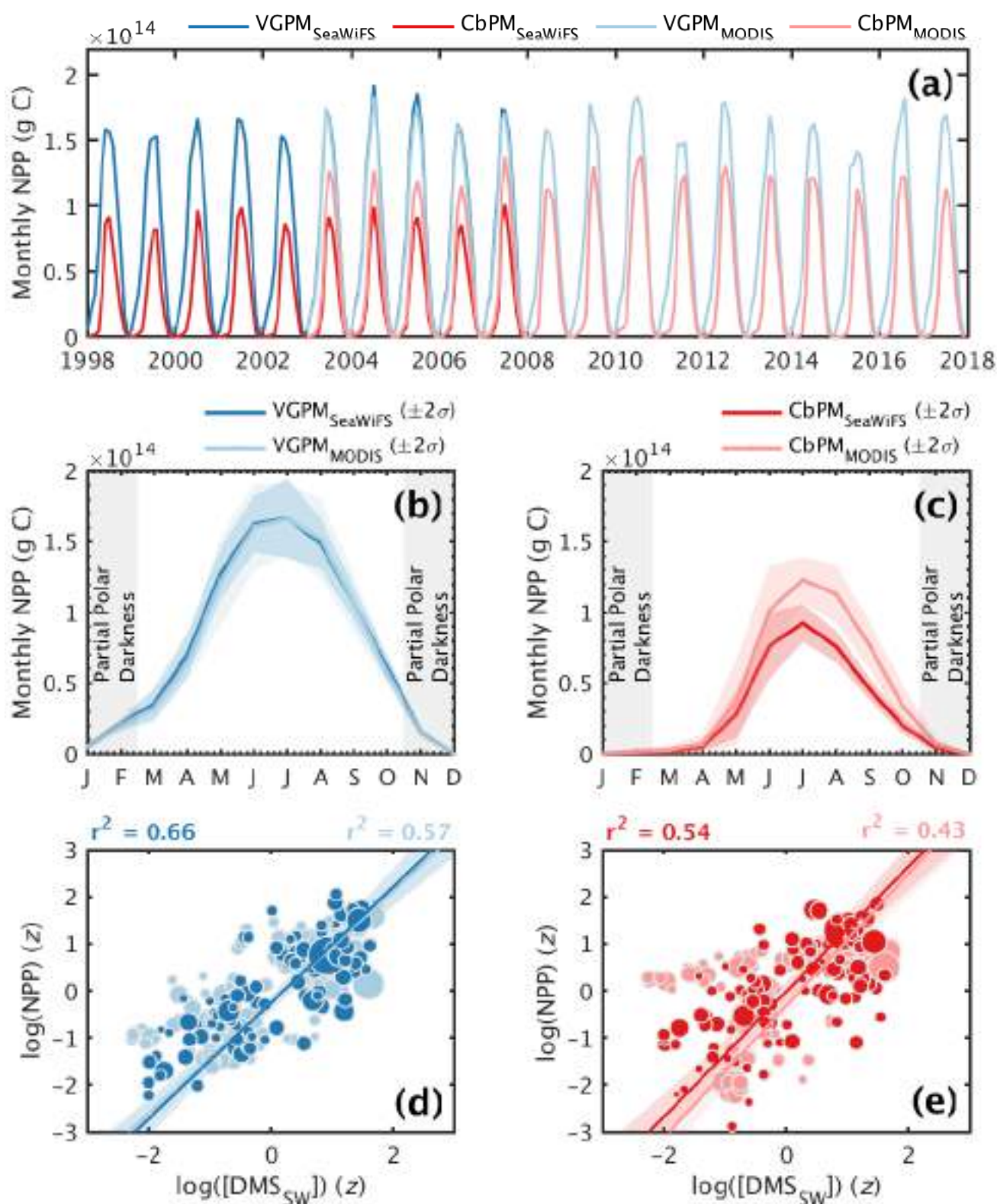
Previously unpublished ice core [MSA] data used in this study (D4, NGT-B16, NGT-B18, NGT-B20, NGT-B21 and NGT-B26) are available via the National Oceanic and Atmospheric Administration (NOAA) Paleoclimatology Data Archive (<https://www.ncdc.noaa.gov/paleo/study/26691>). TUNU, Summit2010, 20D and GC [MSA] data are available via the NSF Arctic Data Center (<http://arcticdata.io>). NGRIP [MSA] data are from ref. ¹⁵. GRIP93a data are from ref. ¹⁸. All [MSA] data are available upon request from the corresponding author. Source Data for Figs. 1, 2, 4 are available in the online version of this paper. Availability of CPR plankton-abundance data is made possible by the Marine Biological Association (<https://www.cprsurvey.org/>; <https://doi.org/10.7487/2018.29.1.1109> and <https://doi.org/10.7487/2018.53.1.1118>). Ocean productivity data are publicly available from <https://www.science.oregonstate.edu/ocean.productivity/>. Ocean [DMS_{SW}] data can be accessed via <https://saga.pmel.noaa.gov/dms/>. The NCEP/NCAR reanalysis data can be downloaded from <https://www.ready.noaa.gov/HYSPLIT.php>.

Code availability

Code used for [MSA] signal extraction, Monte Carlo correlation analysis, HYSPLIT analysis and CPR analysis is available from the corresponding author upon request. Code for SiZer change-point analysis was modified after a previous publication⁴ and is available from the corresponding author upon request. The HYSPLIT source code can be downloaded from <https://www.ready.noaa.gov/HYSPLIT.php>.

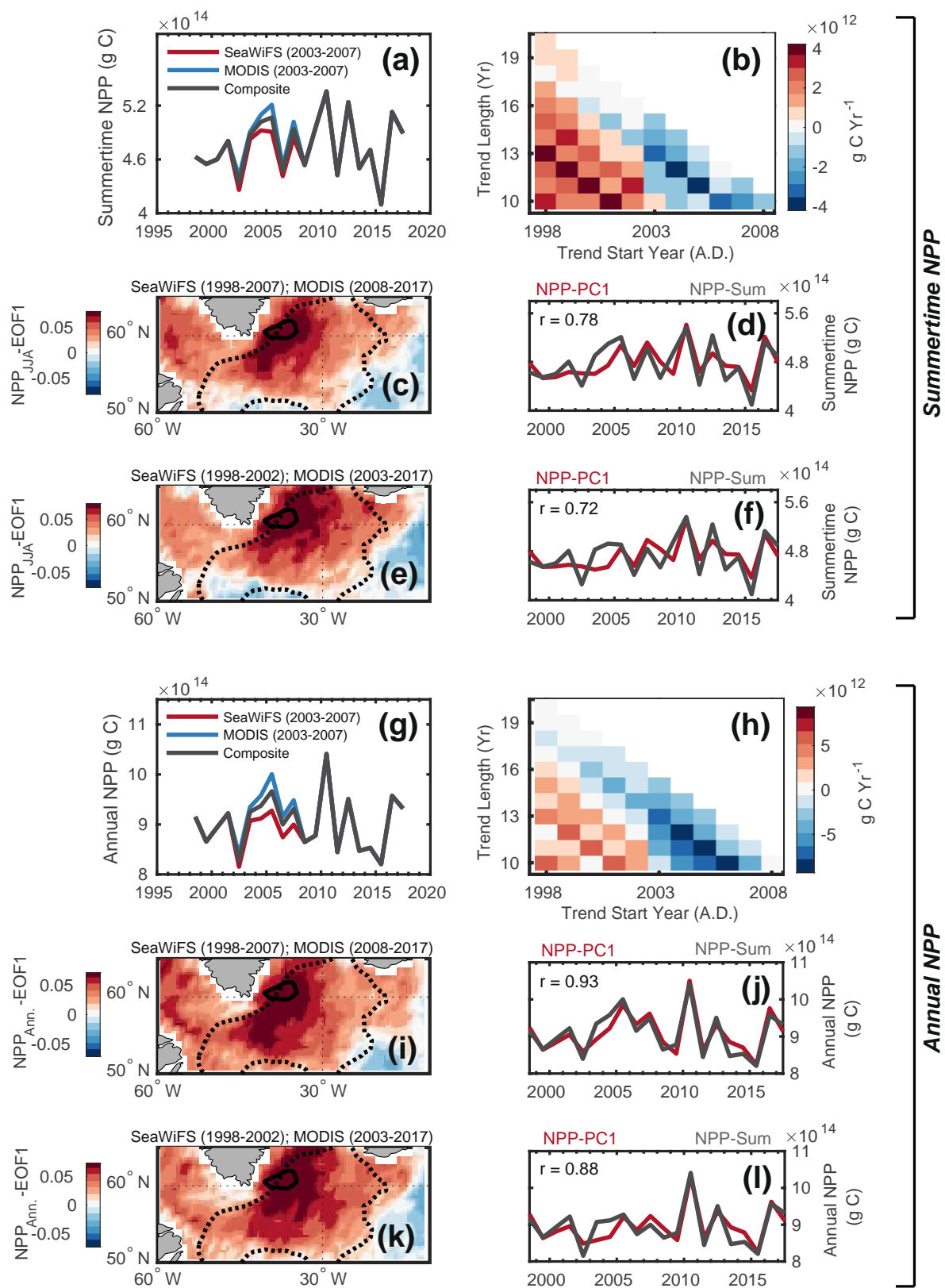
31. Whung, P. Y., Saltzman, E. S., Spencer, M. J., Mayewski, P. A. & Gundestrup, N. Two-hundred-year record of biogenic sulfur in a south Greenland ice core (20D). *J. Geophys. Res.* **99**, 1147–1156 (1994).

32. Saltzman, E. S., Whung, P.-Y. & Mayewski, P. A. Methanesulfonate in the Greenland Ice Sheet Project 2 ice core. *J. Geophys. Res.* **102**, 26649–26657 (1997).
33. North Greenland Ice Core Project members. High-resolution record of Northern Hemisphere climate extending into the last interglacial period. *Nature* **431**, 147–151 (2004).
34. Maselli, O. J. et al. Sea ice and pollution-modulated changes in Greenland ice core methanesulfonate and bromine. *Clim. Past* **13**, 39–59 (2017).
35. Criscitiello, A. S. et al. Ice sheet record of recent sea-ice behavior and polynya variability in the Amundsen Sea, West Antarctica. *J. Geophys. Res.* **118**, 118–130 (2013).
36. Fischer, H., Wagenbach, D. & Kipfstuhl, J. Sulfate and nitrate firn concentrations on the Greenland ice sheet: 1. Large-scale geographical deposition changes. *J. Geophys. Res.* **103**, 21927–21934 (1998).
37. Osman, M., Das, S. B., Marchal, O. & Evans, M. J. Methanesulfonic acid (MSA) migration in polar ice: data synthesis and theory. *Cryosphere* **11**, 2439–2462 (2017).
38. Weller, R. F. et al. Postdepositional losses of methane sulfonate, nitrate, and chloride at the European Project for Ice Coring in Antarctica deep-drilling site in Dronning Maud Land, Antarctica. *J. Geophys. Res.* **109**, D07301 (2004).
39. Mernild, S. H. et al. Greenland precipitation trends in a long-term instrumental climate context (1890–2012): evaluation of coastal and ice core records. *Int. J. Climatol.* **320**, 303–320 (2014).
40. Andersen, K. K. et al. Retrieving a common accumulation record from Greenland ice cores for the past 1800 years. *J. Geophys. Res.* **111**, D15106 (2006).
41. Mosley-Thompson, E., Readinger, C. R., Craigmille, P., Thompson, L. G. & Calder, C. A. Regional sensitivity of Greenland precipitation to NAO variability. *Geophys. Res. Lett.* **32**, L24707 (2005).
42. Beckers, J. M. & Rixen, M. EOF calculations and data filling from incomplete oceanographic datasets. *J. Atmos. Ocean. Technol.* **20**, 1839–1856 (2003).
43. Babamoradi, H., van den Berg, F. & Rinnan, Å. Bootstrap based confidence limits in principal component analysis — a case study. *Chemom. Intell. Lab. Syst.* **120**, 97–105 (2013).
44. Sinclair, K. E., Bertler, N. A., Trompeter, W. J. & Baisden, W. T. Seasonality of air mass pathways to coastal Antarctica: ramifications for interpreting high-resolution ice core records. *J. Clim.* **26**, 2065–2076 (2013).
45. Schlosser, E., Oerter, H., Masson-Delmotte, V. & Reijmer, C. Atmospheric influence on the deuterium excess signal in polar firn: implication for ice-core interpretation. *J. Glaciol.* **54**, 117–124 (2008).
46. Scarchilli, C., Frezzotti, M. & Ruti, P. M. Snow precipitation at four ice core sites in East Antarctica: provenance, seasonality and blocking factors. *Clim. Dyn.* **37**, 2107–2125 (2011).
47. Sharma, S. et al. Influence of transport and ocean ice extent on biogenic aerosol sulfur in the Arctic atmosphere. *117*, D12209 (2012).
48. Hezel, P. J. et al. Modeled methanesulfonic acid (MSA) deposition in Antarctica and its relationship to sea ice. *J. Geophys. Res.* **116**, D23214 (2011).
49. Criscitiello, A. S. et al. Marine aerosol source regions to Prince of Wales Icefield, Ellesmere Island, and influence from the tropical Pacific, 1979–2001. *J. Geophys. Res.* **121**, 9492–9507 (2016).
50. Stein, A. F. et al. NOAA's HYSPLIT atmospheric transport and dispersion modeling system. *Bull. Am. Meteorol. Soc.* **96**, 2059–2077 (2015).
51. Kalnay, E. et al. The NCEP/NCAR 40-year reanalysis project. *Bull. Am. Meteorol. Soc.* **77**, 437–471 (1996).
52. Kettle, A. J. et al. A global database of sea surface dimethylsulfide (DMS) measurements and a procedure to predict sea surface DMS as a function of latitude, longitude, and month. *Glob. Biogeochem. Cycles* **13**, 399–444 (1999).
53. Richardson, A. J. et al. Using continuous plankton recorder data. *Prog. Oceanogr.* **68**, 27–74 (2006).
54. Jonas, T. D. et al. The volume of water filtered by a continuous plankton recorder sample: the effect of ship speed. *J. Plankton Res.* **26**, 1499–1506 (2004).
55. Ebisuzaki, W. A method to estimate the statistical significance of a correlation when the data are serially correlated. *J. Clim.* **10**, 2147–2153 (1997).
56. Hannig, J. & Marron, J. S. Advanced distribution theory for SiZer. *J. Am. Stat. Assoc.* **101**, 484–499 (2006).
57. Westberry, T., Behrenfeld, M. J., Siegel, D. A. & Boss, E. Carbon-based primary productivity modeling with vertically resolved photoacclimation. *Glob. Biogeochem. Cycles* **22**, GB2024 (2008).
58. Rayner, N. A. et al. Global analyses of sea surface temperature, sea ice, and night marine air temperature since the late nineteenth century. *J. Geophys. Res.* **108**, 4407 (2003).
59. Josey, S. A. et al. The recent Atlantic cold anomaly: causes, consequences, and related phenomena. *Ann. Rev. Mar. Sci.* **10**, 475–501 (2018).
60. McConnell, J. R. et al. 20th-century industrial black carbon emissions altered Arctic climate forcing. *Science* **317**, 1381–1384 (2007).
61. Weißbach, S. et al. Spatial and temporal oxygen isotope variability in northern Greenland — implications for a new climate record over the past millennium. *Clim. Past* **12**, 171–188 (2016).



Extended Data Fig. 1 | Comparison of NPP products. **a**, Monthly integrated NPP (g C) across the subarctic Atlantic (50–65° N, 60–10° W, see also yellow boxed region in Fig. 3a) for the SeaWiFS-VGPM and MODIS-VGPM NPP products¹², as well as an independently derived SeaWiFS-carbon-based productivity model⁵⁷ (CbPM) (Supplementary Information) and MODIS-CbPM NPP products. **b**, **c**, SeaWiFS- and MODIS-derived NPP mean seasonality ($\pm 2\sigma$; $n = 20$ years; January 1998–December 2017) for the VGPM (**b**) and CbPM (**c**) datasets. Note

that four months—November–December–January–February—experience partial polar darkness over the subarctic Atlantic latitude bands (50–65° N), leading to systematic underestimates of productivity during these months. **d**, **e**, VGPM-based (**d**) and CbPM-based (**e**) linear regressions with ship-based $[\text{DMS}_{\text{SW}}]$ measurements (similar to Fig. 3b; see Methods) using the MODIS and SeaWiFS NPP datasets. Shaded bands show the 95% confidence interval of the regression. Regression values (r^2) represent the squared Pearson product-moment coefficients.

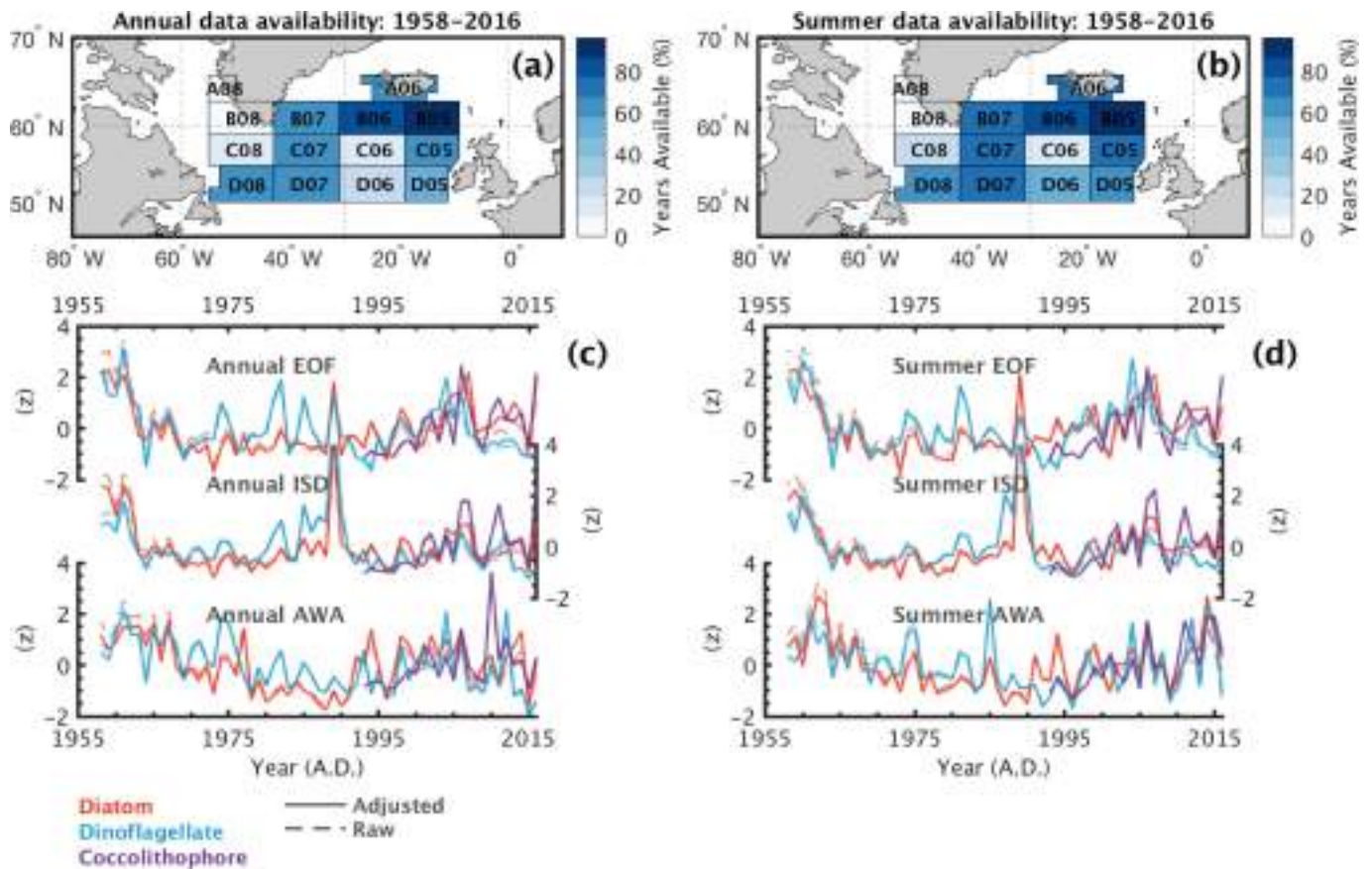


Extended Data Fig. 2 | See next page for caption.

Extended Data Fig. 2 | Seasonal representativeness of subarctic Atlantic VGPM NPP satellite-era trends and sensitivity to satellite sensor used.

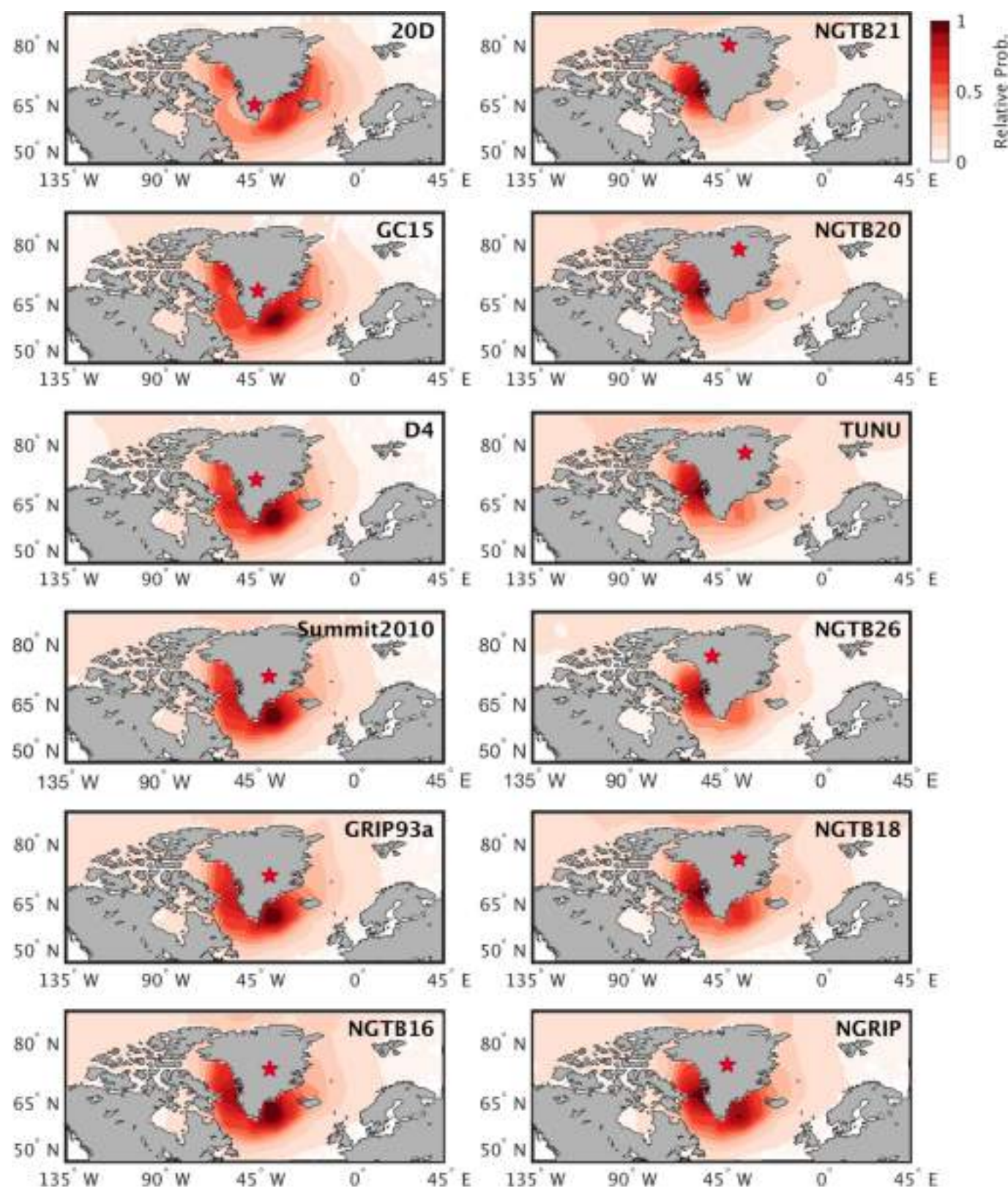
a, Comparison of summertime-integrated (JJA) subarctic Atlantic VGPM NPP yields for three different sensor estimates: a SeaWiFS-dominant estimate (red; 1998–2007 NPP estimates derived from the SeaWiFS sensor and 2008–2017 NPP estimates from the MODIS sensor), a MODIS-dominant estimate (blue; SeaWiFS-based data for 1998–2002 and MODIS-based data for 2003–2017), and the composite stack (dark grey; comprising the average of SeaWiFS- and MODIS-derived summertime VGPM NPP estimates over their period of common annual

overlap, 2003–2007). **b**, Differential linear trend analysis of the composite summertime subarctic Atlantic NPP time series from **a**. No decadal-scale linear trends were found to be significant at $P < 0.05$, using a two-sided Student's t -test with $n - 2$ degrees of freedom (where n represents the varying trend length in years). **c**, **d**, EOF1 (**c**) and PC1 (**d**) of summertime VGPM NPP using the MODIS-dominant dataset, similar to Fig. 3c, d, respectively. **e**, **f**, As in **c**, **d**, but showing EOF results from the SeaWiFS-dominant summertime VGPM NPP dataset. **g**–**i**, As in **a**–**f**, but showing annually integrated VGPM NPP estimates. All regression values (r) represent Pearson product-moment coefficients.



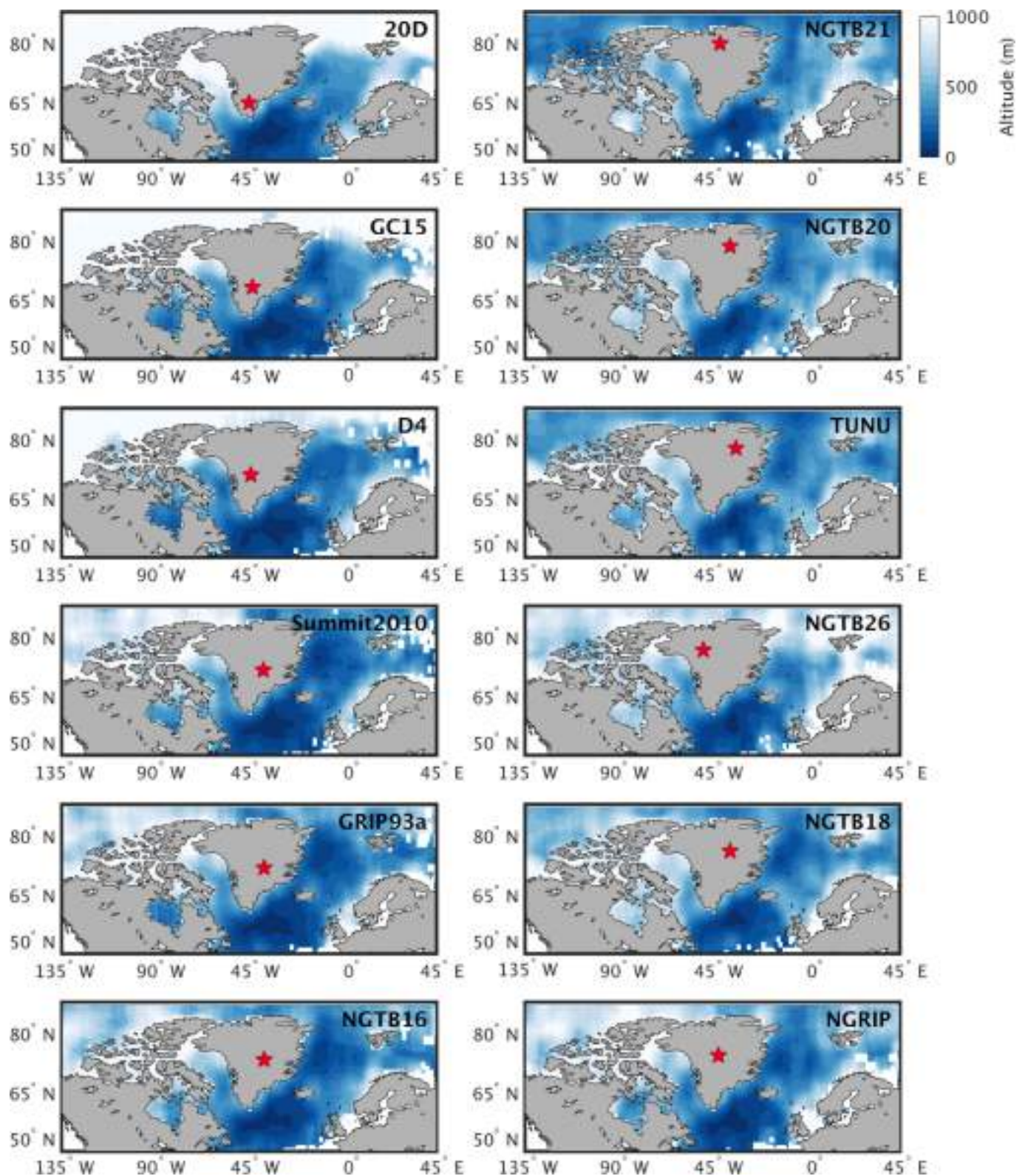
Extended Data Fig. 3 | Comparison of subarctic Atlantic CPR compositing techniques. **a, b**, Data availability (AD 1958–2016) by CPR standard region (Methods) for annually derived (**a**; ≥ 8 out of 12 months per year of data required) and summertime-derived (**b**; ≥ 4 out of 6 months per year during April–May–June–July–August–September) data. **c, d**, Three approaches for compositing time series of CPR-based planktonic abundance, for both annual (**c**) and summertime (**d**) data⁴²

(see Supplementary Information). AWA, area-weighted averaging; ISD, inverse-squared distance-based data infilling; EOF, EOF-based data infilling. Thin dashed lines show standardized (z -score units relative to AD 1958–2016) raw annual relative abundances of plankton; bold lines show adjusted relative abundances, to correct for potential long-term biases in the volume of water sampled by CPR devices^{53,54}. Note that the annual area-weighted averaged series is reproduced from Fig. 4a.



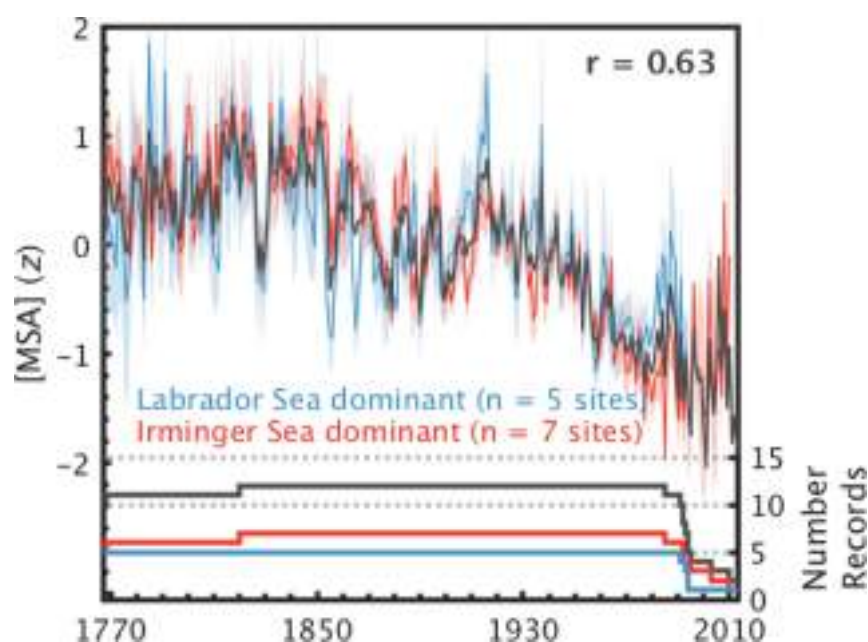
Extended Data Fig. 4 | HYSPLIT-computed summertime (JJA) air mass transport probability densities for each ice core site. Site-specific JJA marine-air mass transport density maps, representing the relative probability of an oceanic air mass passing through a given atmospheric column before its arrival at each site. All marine-air mass transport density maps are computed over the period AD 1 January 1948 to 31 December

2013 (that is, 6,121 JJA trajectories per site) and normalized on a 0–1 relative scale with 1 and 0 indicating the most and least probable air mass trajectory grid point, respectively. Sites are shown anticlockwise from most southerly (20D; top left) to most northerly (NGTB21; top right) situated on the GrIS.



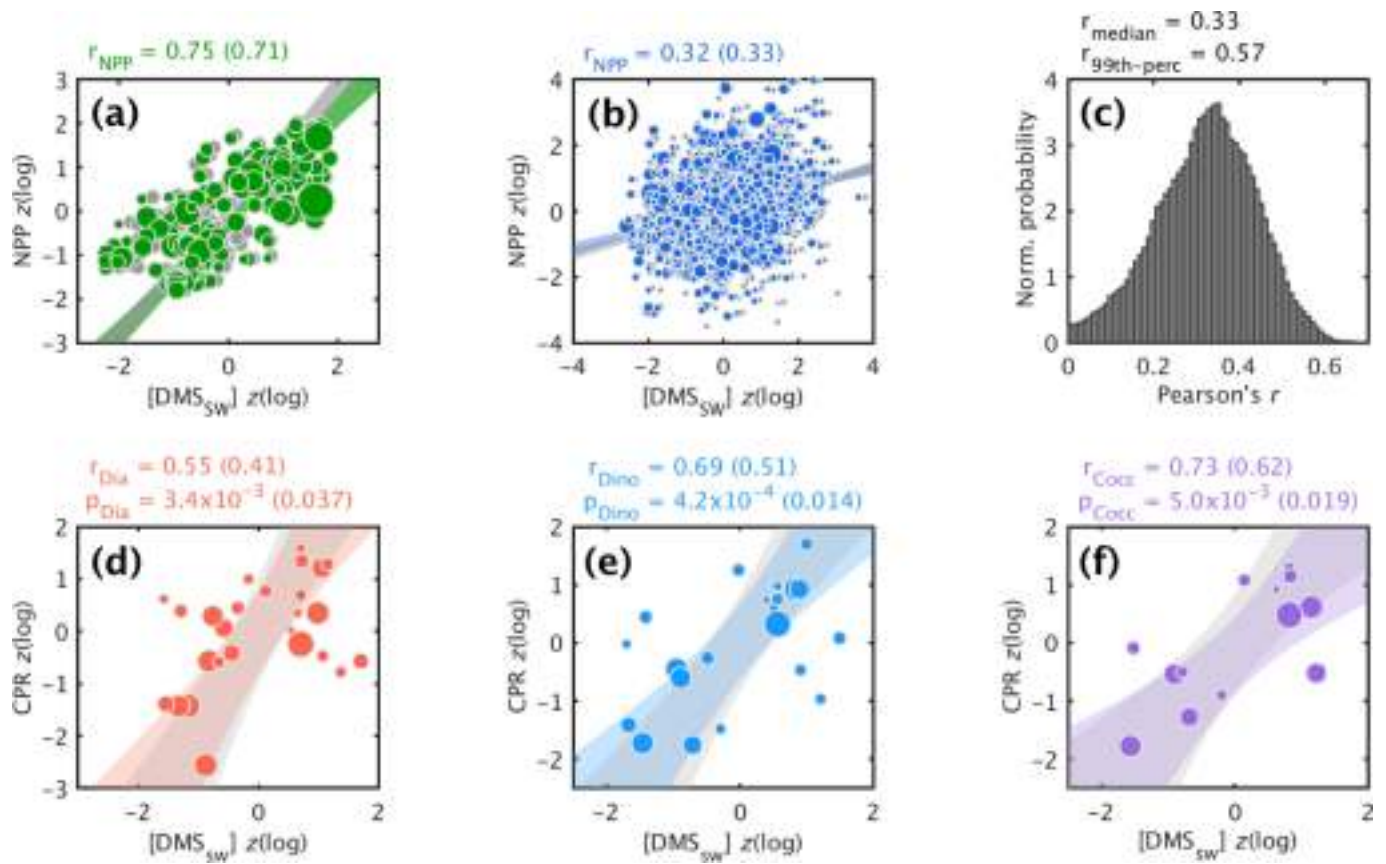
Extended Data Fig. 5 | HYSPLIT-computed summertime (JJA) airmass median elevation maps for each ice core site. Site-specific median atmospheric altitudes (m above sea level) for all ocean-situated JJA hourly trajectory locations over the period AD 1948–2013. All maps were

computed over the period AD 1 January 1948 to 31 December 2013 (that is, 6,121 JJA trajectories per site). Sites are shown anticlockwise from most southerly (20D; top left) to most northerly (NGTB21; top right) situated on the GrIS.



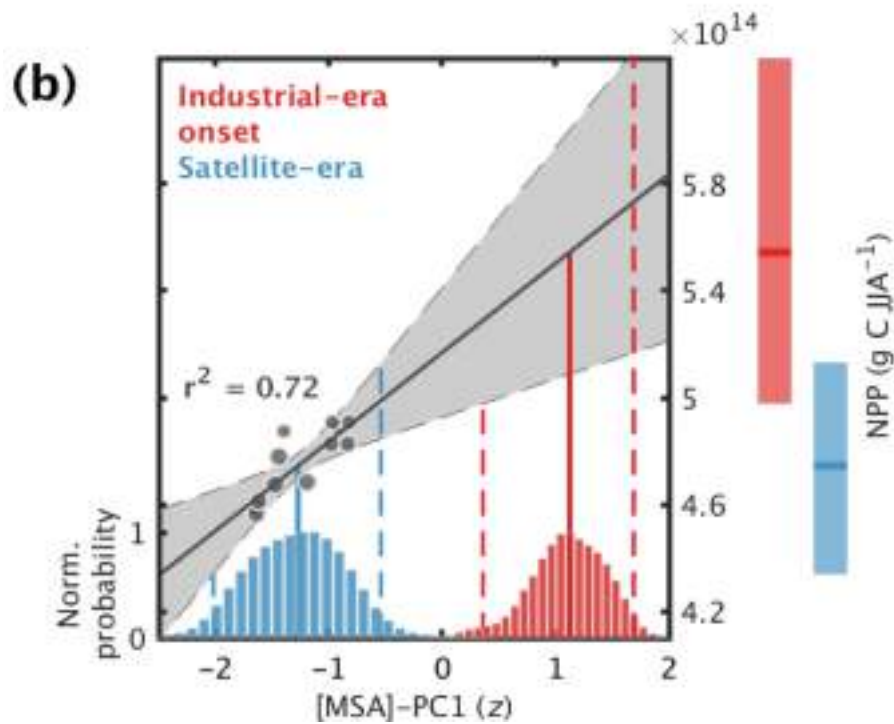
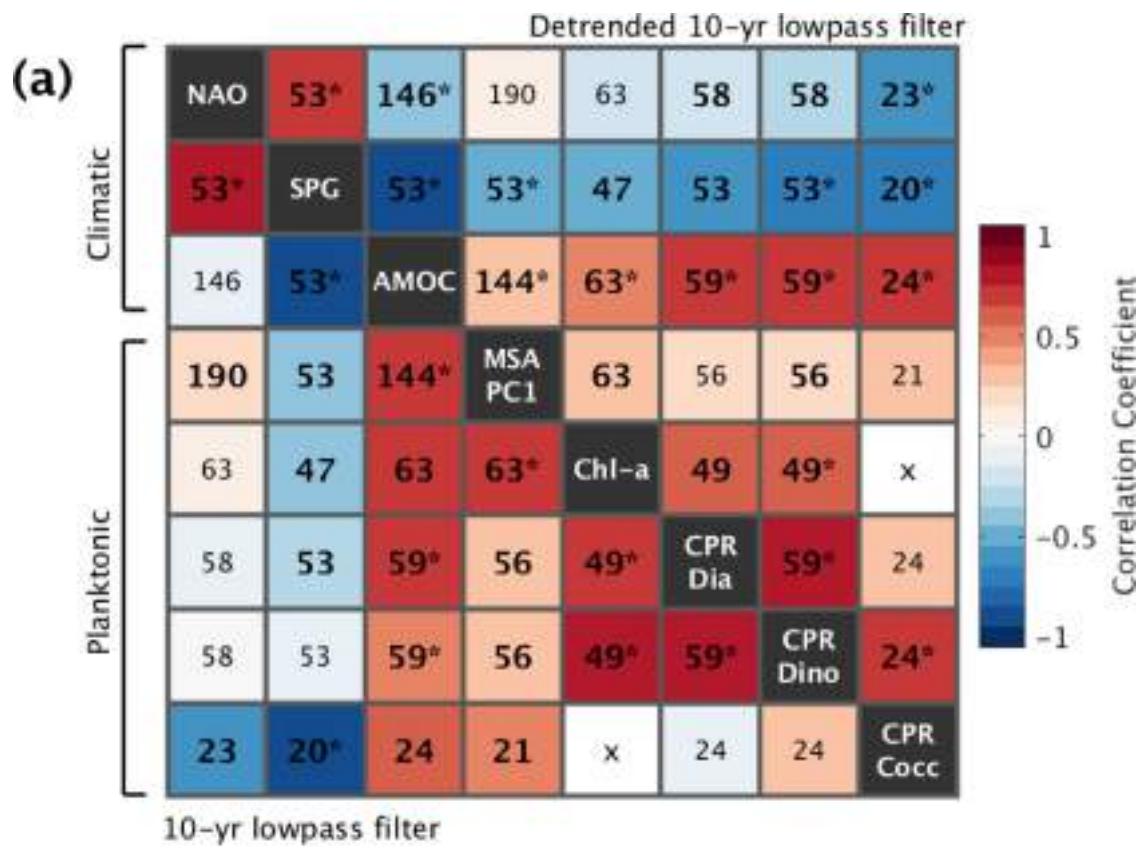
Extended Data Fig. 6 | Strong covariation between two [MSA] source-trajectory regions. Top, the 12 Greenland [MSA] records from Fig. 1a annually averaged across the two air-mass-trajectory factor analysis groupings from Fig. 1b ($r = 0.63$, $P < 0.0001$); the r value represents the Pearson product-moment coefficient. All records have been standardized

(z units) relative to their period of common overlap (AD 1821–1985). The shaded bands show ± 1 s.e.m. about the stack means. The grey line shows the composite (12-site) mean. Bottom, [MSA] record availability over time.



Extended Data Fig. 7 | Relation between $[DMS_{SW}]$, NPP and CPR planktonic abundance. **a**, Reproduced from Fig. 3b. **b**, As in **a**, but for globally regressed values. The diameter of the circles represents the root of the relative weighting (inverse standard error of the $[DMS_{SW}]$ measurement) used in the weighted least squares (WLS) regressions ($n_{WLS,subarctic} = 184$; $n_{WLS,global} = 2,219$ degrees of freedom). Grey circles represent points used in the ordinary least squares (OLS) regression ($n_{OLS,subarctic} = 222$; $n_{OLS,global} = 3,043$). **c**, Probability density of global r values over $i = 1, 2, \dots, 10,000$ degrees-of-freedom preserving (that is, $n_i = 184$) bootstrap WLS regressions (Supplementary Information).

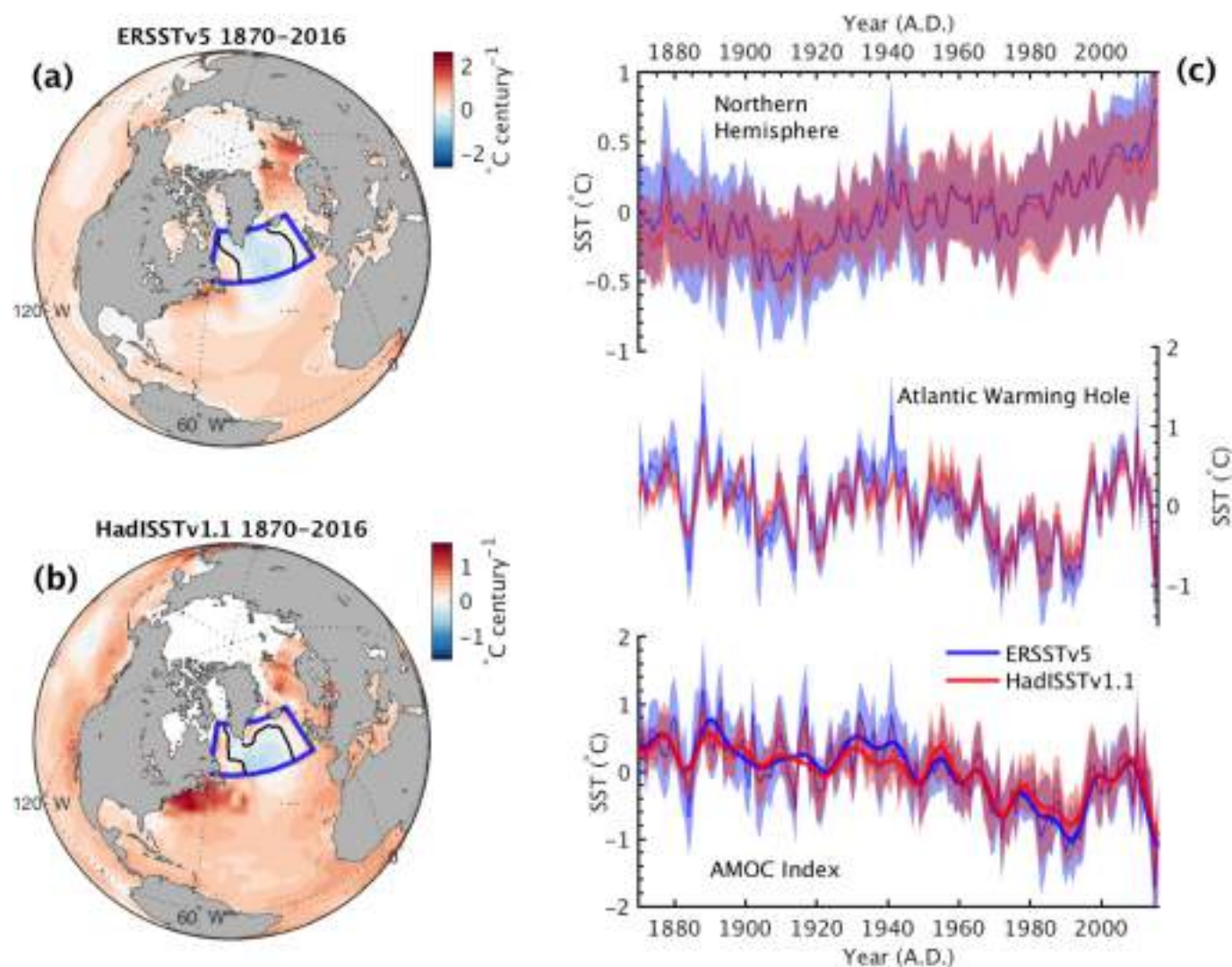
d–f, Linear regression analyses of subarctic Atlantic $[DMS_{SW}]$ versus CPR-based abundances of diatoms (**d**), dinoflagellates (**e**) and coccolithophores (**f**). In all regressions, the coloured or grey shaded regions denote the 95% confidence intervals around the regression parameters for the WLS or OLS regressions, respectively. All WLS and OLS regressions were significant at $P < 0.005$ and $P < 0.05$, respectively, assuming a two-tailed Student's t -distribution with a t -statistic representing $n - 2$ degrees of freedom. Regression values (r) represent Pearson product-moment coefficients.



Extended Data Fig. 8 | See next page for caption.

Extended Data Fig. 8 | Industrial-era decline in subarctic Atlantic NPP and climatic influence. **a**, Correlation matrix (Pearson product-moment coefficients, r) of planktonic and observed-climatic indices from Fig. 4a. Integers represent n , the years of overlap between paired series. Bold n values represent significance at the 90% confidence level ($P < 0.1$; assuming a two-tailed Student's t -distribution with a t -statistic representing $n - 2$ degrees of freedom). Bold n values with an asterisk represent significance using a Monte Carlo-based Fourier phase-randomization procedure, a more stringent test to account for serial correlation (and hence varying degrees of freedom) among paired series (Methods). All 10-year low-pass-filtered (bottom left of diagonal), and linearly detrended 10-year low-pass-filtered (top right of diagonal), series convolved using a Gaussian filter. Paired series with less than 20 years of

overlap are denoted missing with an 'x'. **b**, WLS model of 5-year smoothed [MSA] PC1 and summertime NPP PC1 ($n = 12$ years; $r^2 = 0.72$; $P = 0.04$ after adjusting for reduced degrees of freedom; Methods). The regression weights are the inverse 1σ of [MSA] PC1 values. Histogram distributions denote the range of industrial-era onset and satellite-era [MSA] PC1 values following 10,000 bootstrap tests (distributions normalized to their maximum). The shaded band shows the 95% confidence interval of the WLS regression parameters. The corresponding 95% confidence ranges of NPP rates (g C per JJA) over the industrial-era onset and satellite era are shown to the right. The analysis suggests an average decline of approximately $14 \pm 11\%$ (mean $\pm 2\sigma$) in summertime-integrated NPP yields since the industrial-era onset.



Extended Data Fig. 9 | Subarctic Atlantic SST analysis. **a, b**, Annual SST linear trends in the ERSST v.5³⁰ (**a**) and HadISST v.1.1⁵⁸ (**b**) reanalyses. Grid points exhibiting a 147-year (AD 1870–2016) cooling trend within the subarctic Atlantic (50–65° N; 60–10° W; bold blue outline) are outlined by black isopleths and defined to encompass the Atlantic warming hole⁵⁹. **c**, ERSST and HadISST anomalies (mean-centred relative

to AD 1870–2016; $n = 147$ years) for the Northern Hemisphere (top; $\pm\sigma$), the Atlantic warming hole (middle; $\pm\sigma$) and the difference between warming hole and Northern Hemisphere SSTs, representing the AMOC index as approximately defined previously^{6,7} (bottom; $\pm\sigma$). Bold AMOC time series are 10-year (Butterworth) low-pass-filtered data.

Extended Data Table 1 | Geographical, physical and glaciological information pertaining to each ice core [MSA] record

| Site name | Site ID (Fig. 1) | Lat/Lon | Elevation (m) | SAT (°C) | \dot{b} (m w.e. yr ⁻¹) | Core length (m) | Time period (A.D.) | Peak [MSA] seasonality (0–10 m) | Mean [MSA] ($\pm 1\sigma$; $\mu\text{g L}^{-1}$) | $r_{[\text{MSA}]/\text{PC1}}$ (p) | Reference |
|------------|------------------|---------------------|---------------|----------|--------------------------------------|-----------------|--------------------|---------------------------------|---|---------------------------------------|------------------------|
| 20D | 1 | 65.01°N -44.87°W | 2615 | n/a | 0.410 | 116 | 1767–1985 | Jun-Aug | 3.28 (1.02) | 0.300 (0.038) | Ref. 15, 31 |
| GC | 2 | 68.91°N -43.39°W | 2465 | -24 | 0.360 | 104 | 1821–2013 | Jul-Sep | 1.62 (0.61) | 0.410 ($<1 \times 10^{-4}$) | This study; Ref. 16 |
| D4 | 3 | 71.67°N -44.00°W | 2715 | -26 | 0.420 | 145 | 1733–2004 | Jun-Jul | 2.31 (0.92) | 0.766 ($<1 \times 10^{-4}$) | This study; Ref. 60 |
| Summit2010 | 4 | 72.33°N -38.29°W | 3215 | -29.3 | 0.220 | 87 | 1742–2010 | May-Jun | 3.57 (0.94) | 0.851 ($<1 \times 10^{-4}$) | Ref. 34 |
| GRIP93a | 5 | 72.57°N -37.63°W | 3240 | -31.5 | 0.200– 0.220 | 73 | 1767–1993 | Jul-Sep | 3.02 (1.01) | 0.712 ($<1 \times 10^{-4}$) | Ref. 18 |
| NGT-B16 | 6 | 73.94°N -37.63°W | 3040 | -32.5* | 0.134– 0.148 | 102 | 1483–1991 | n/a | 2.57 (0.63) | 0.745 ($<1 \times 10^{-4}$) | This study; Ref. 61 |
| NGRIP | 7 | 75.1°N -42.32°W | 2950 | -30.2 | – | – | 187–1995 | n/a | 3.12 (1.08) | 0.725 ($<1 \times 10^{-4}$) | Ref. 15; 33 |
| NGT-B18 | 8 | 76.62°N -36.40°W | 2508 | -32.3* | 0.100– 0.110 | 84 | 1443–1993 | n/a | 1.60 (0.38) | 0.792 ($<1 \times 10^{-4}$) | This study; Ref. 61 |
| NGT-B26 | 9 | 77.25°N -49.22°W | 2598 | -30.3* | 0.172– 0.190 | 88 | 1502–1995 | n/a | 0.94 (0.42) | 0.563 ($<1 \times 10^{-4}$) | This study; Ref. 61 |
| TUNU | 10 | 78.03°N -33.87°W | 2120 | -27.5 | 0.110 | 213 | 269–2013 | Jul-Aug | 2.12 (0.53) | 0.273 (5.6×10^{-9}) | Ref. 34 |
| NGT-B20 | 11 | 78.83°N -36.50°W | 2147 | -30.4* | 0.90– 0.105 | 120 | 1066–1994 | n/a | 0.88 (0.44) | 0.315 (7.2×10^{-9}) | This study; Ref. 61 |
| NGT-B21 | 12 | 80.00°N -41.41°W | 2185 | -30.1* | 0.105– 0.113 | 94 | 1395–1993 | n/a | 2.28 (0.42) | 0.282 (0.091) | This study; Ref. 61 |

The annual site mean $\pm \sigma$ [MSA] values for the period of common overlap between records are shown as indicated for AD 1821–1985 ($n = 165$ years). The homogenous correlations (Pearson r) and significance level⁵⁵ (p) between [MSA] PC1 and the 12 GrIS [MSA] records comprising it are shown, computed over the period of common overlap. Note that correlation values are reproduced from colour-coded values shown in the inset map of Fig. 2a. This table cites refs. 15,16,18,31,33,34,60,61 from this study.

Reporting Summary

Nature Research wishes to improve the reproducibility of the work that we publish. This form provides structure for consistency and transparency in reporting. For further information on Nature Research policies, see [Authors & Referees](#) and the [Editorial Policy Checklist](#).

Statistics

For all statistical analyses, confirm that the following items are present in the figure legend, table legend, main text, or Methods section.

n/a Confirmed

- ☐ ☒ The exact sample size (n) for each experimental group/condition, given as a discrete number and unit of measurement
- ☐ ☒ A statement on whether measurements were taken from distinct samples or whether the same sample was measured repeatedly
- ☐ ☒ The statistical test(s) used AND whether they are one- or two-sided
Only common tests should be described solely by name; describe more complex techniques in the Methods section.
- ☐ ☒ A description of all covariates tested
- ☐ ☒ A description of any assumptions or corrections, such as tests of normality and adjustment for multiple comparisons
- ☐ ☒ A full description of the statistical parameters including central tendency (e.g. means) or other basic estimates (e.g. regression coefficient) AND variation (e.g. standard deviation) or associated estimates of uncertainty (e.g. confidence intervals)
- ☐ ☒ For null hypothesis testing, the test statistic (e.g. F , t , r) with confidence intervals, effect sizes, degrees of freedom and P value noted
Give P values as exact values whenever suitable.
- ☒ ☐ For Bayesian analysis, information on the choice of priors and Markov chain Monte Carlo settings
- ☒ ☐ For hierarchical and complex designs, identification of the appropriate level for tests and full reporting of outcomes
- ☒ ☐ Estimates of effect sizes (e.g. Cohen's d , Pearson's r), indicating how they were calculated

Our web collection on [statistics for biologists](#) contains articles on many of the points above.

Software and code

Policy information about [availability of computer code](#)

Data collection

No software was used for data collection.

Data analysis

All MATLAB (tested up to R2015a) code used for methanesulfonic acid data reduction and Monte Carlo correlation analysis is available from M.B.O. upon request. MATLAB code for SiZer change-point analysis was modified after ref. 4 (<https://www.nature.com/articles/nature19082>) and is available from M.B.O. upon request. The HYSPLIT source-code and supporting NCAR-NCEP reanalysis data is publicly available and can be downloaded at <https://www.ready.noaa.gov/HYSPLIT.php>.

For manuscripts utilizing custom algorithms or software that are central to the research but not yet described in published literature, software must be made available to editors/reviewers. We strongly encourage code deposition in a community repository (e.g. GitHub). See the Nature Research [guidelines for submitting code & software](#) for further information.

Data

Policy information about [availability of data](#)

All manuscripts must include a [data availability statement](#). This statement should provide the following information, where applicable:

- Accession codes, unique identifiers, or web links for publicly available datasets
- A list of figures that have associated raw data
- A description of any restrictions on data availability

Annual ice core [MSA] data used in this study are being made available via the NSF Arctic Data Center (<http://arcticdata.io>). Additionally, source data for Figures 1, 2, and 4 are available in the online version of this paper. Code used for [MSA] signal extraction, Monte Carlo correlation analysis, and CPR analysis is available from M.B.O. upon request. Code for SiZer change-point analysis was modified after ref. 4 (<https://www.nature.com/articles/nature19082>) and is available from M.B.O. upon request. Availability of CPR plankton-abundance data is made possible by the Sir Alistar Hardy Foundation for Ocean Science (<https://www.cprsurvey.org/>; doi:10.7487/2018.29.1.1109 and doi:10.7487/2018.53.1.1118). Ocean productivity data are publicly available from <https://www.science.oregonstate.edu/ocean.productivity/>. Ocean [DMSSW] data can be accessed via <https://saga.pmel.noaa.gov/dms/>. The HYSPLIT source-code and NCAR-NCEP reanalysis data can be downloaded at <https://www.ready.noaa.gov/HYSPLIT.php>.

Field-specific reporting

Please select the one below that is the best fit for your research. If you are not sure, read the appropriate sections before making your selection.

☐ Life sciences ☐ Behavioural & social sciences ☒ Ecological, evolutionary & environmental sciences

For a reference copy of the document with all sections, see [nature.com/documents/nr-reporting-summary-flat.pdf](https://www.nature.com/documents/nr-reporting-summary-flat.pdf)

Ecological, evolutionary & environmental sciences study design

All studies must disclose on these points even when the disclosure is negative.

| | |
|-----------------------------------|---|
| Study description | We reconstruct oceanic primary productivity variations across the subarctic Atlantic basin over the last 250 years using twelve methanesulfonic acid concentration (MSA) ice core records from sites situated across the Greenland Ice Sheet. |
| Research sample | Five of the twelve MSA records are previously published (Extended Data Table 1 and references therein). Analytical procedures and dating methodologies used to produce the remaining seven MSA records are listed in Extended Data Table 1 and references therein. Supporting ship- and satellite-based planktonic data sources, each publicly-available, are listed in the "Data" section above. |
| Sampling strategy | Greenland Ice Sheet MSA records were selected under the criterion that each record i) be of moderate to high temporal resolution (measured at <3 years per sample), ii) come from well-dated ice cores (<5 year estimated uncertainty at the oldest portions of the core), and iii) represent >100 years of continuous length. |
| Data collection | No ice cores used in our study are novel (see also "Research sample", above). Specific details on the collection of each core can be found within the references listed in Extended Data Table 1. |
| Timing and spatial scale | The 12 ice core MSA records used to generate our ice core productivity index span the Greenland Ice Sheet, with specific geographic and time-coverage information on each provided in Extended Data Table 1. Each record was analyzed for MSA using well-established trace-chemistry methods at high temporal resolution (generally less than one year per sample) with details included in the Methods and references therein. |
| Data exclusions | No ice core MSA or CPR-survey planktonic abundance data were excluded. Rationale behind the exclusion of extreme-percentile (i.e., <2.5th and >97.5th percentiles) ocean DMS concentration data is provided in the Methods section. |
| Reproducibility | All MSA measurements and software used in developing our ice core-based productivity index are being made public and (or) available upon request from the corresponding author. All supporting-data (as well as software-used to analyze these data) are derived from publicly-available sources (see "Software and code" and "Data" sections, above). |
| Randomization | This study does not include experimental groups. Random sampling with replacement of the 12 MSA records (i.e., "bootstrap" sampling; n = 10,000 iterations) was used for characterizing confidence limits in our ice core productivity index (see Methods). |
| Blinding | Blinding experiments were not applicable for our study. Ice core data reported are based on quantitative trace-chemistry measurements (see Methods). |
| Did the study involve field work? | <input type="checkbox"/> Yes <input checked="" type="checkbox"/> No |

Reporting for specific materials, systems and methods

We require information from authors about some types of materials, experimental systems and methods used in many studies. Here, indicate whether each material, system or method listed is relevant to your study. If you are not sure if a list item applies to your research, read the appropriate section before selecting a response.

Materials & experimental systems

| | |
|-------------------------------------|--|
| n/a | Involved in the study |
| <input checked="" type="checkbox"/> | <input type="checkbox"/> Antibodies |
| <input checked="" type="checkbox"/> | <input type="checkbox"/> Eukaryotic cell lines |
| <input checked="" type="checkbox"/> | <input type="checkbox"/> Palaeontology |
| <input checked="" type="checkbox"/> | <input type="checkbox"/> Animals and other organisms |
| <input checked="" type="checkbox"/> | <input type="checkbox"/> Human research participants |
| <input checked="" type="checkbox"/> | <input type="checkbox"/> Clinical data |

Methods

| | |
|-------------------------------------|---|
| n/a | Involved in the study |
| <input checked="" type="checkbox"/> | <input type="checkbox"/> ChIP-seq |
| <input checked="" type="checkbox"/> | <input type="checkbox"/> Flow cytometry |
| <input checked="" type="checkbox"/> | <input type="checkbox"/> MRI-based neuroimaging |